

pubs.acs.org/acssensors Article

Novel Gas Sensing Approach: ReS₂/Ti₃C₂T_x Heterostructures for NH₃ Detection in Humid Environments

Sahil Gasso, Jake Carrier, Daniela Radu, and Cheng-Yu Lai*



Cite This: ACS Sens. 2024, 9, 4788-4802



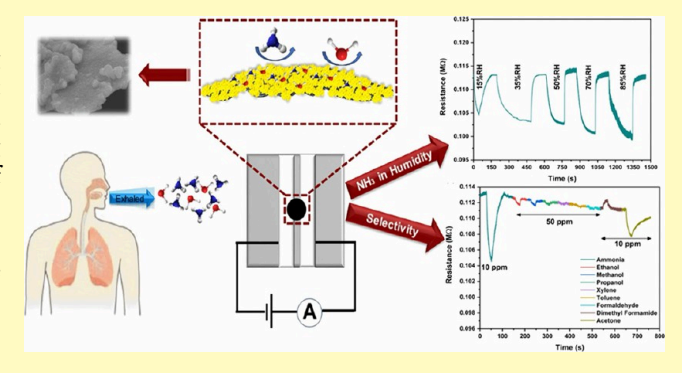
ACCESS I

III Metrics & More

Article Recommendations

s Supporting Information

ABSTRACT: Continuous monitoring of ammonia (NH₃) in humid environments poses a notable challenge for gas sensing applications because of its effect on sensor sensitivity. The present work investigates the detection of NH₃ in a natural humid environment utilizing ReS₂/Ti₃C₂T_x heterostructures as a sensing platform. ReS₂ nanosheets were vertically grown on the surface of Ti₃C₂T_x sheets through a hydrothermal synthetic approach, resulting in the formation of ReS₂/Ti₃C₂T_x heterostructures. The structural, morphological, and optical properties of ReS₂/Ti₃C₂T_x were investigated using various state-of-the-art techniques, including scanning electron microscopy, transmission electron microscopy, X-ray diffraction, X-ray photoelectron spectroscopy, zeta potential, Brunauer–Emmett–Teller technique, and Raman



spectroscopy. The heterostructures exhibited 1.3- and 8-fold increases in specific surface area compared with ReS₂ and $Ti_3C_2T_x$, respectively, potentially enhancing the active gas adsorption sites. The electrical investigations of the ReS₂/ $Ti_3C_2T_x$ -based sensor demonstrated enhanced selectivity and superior sensing response ranging from 7.8 to 12.4% toward 10 ppm of NH₃ within a relative humidity range of 15–85% at room temperature. These findings highlight the synergistic effect of ReS₂ and $Ti_3C_2T_x$, offering valuable insights for NH₃ sensing in environments with high humidity, and are explained in the gas sensing mechanism.

KEYWORDS: ReS₂, MXene, ammonia, humidity, heterostructures

ver the past decade, global advancements in industry and agriculture have resulted in air pollution levels detrimental to both human health and the environment, caused primarily by release of a range of toxic gases, including ammonia (NH₃), nitrogen dioxide (NO₂), carbon dioxide (CO₂), methane (CH₄), hydrogen sulfide (H₂S), and sulfur dioxide (SO₂) into the atmosphere. Among these gases, NH₃, a colorless, corrosive, water-soluble, and lightweight gas with a pungent odor, is one of the most toxic ones. 1,2 Approximately 80% of NH₃ is dedicated to nitrogen-based fertilizer production, with the remaining 20% serving purposes in pharmaceuticals, water purification, refrigeration, explosives, and cleaning products.³ Additionally, NH₃ finds daily application in dairy and ice cream plants, wineries and breweries, petrochemical facilities, fruit and vegetable juice processing, and soft drink manufacturing.4 Due to its widespread use, NH3 poses significant environmental and health risks, ranging from eye and nose irritation to chest pain, lung edema, bronchitis, and death in some cases. 5,6 Considering the toxicity and safety concerns, global health authorities have established a restriction of 25 and 35 ppm to long- and short-term exposure times of 8 h and 10 min, respectively, to safeguard human health.7 Given the diverse applications of NH3 and associated health risks, there is an imperative need for monitoring even a trace of NH3 at room

temperature. Also, NH₃ assumes a pivotal role in the realm of medical applications, serving as a biomarker for kidney and liver disorders, thus enabling the early detection of cancer within the human body. Thus, the detection of low NH₃ concentrations in humid environments is paramount for ensuring public safety, facilitating air quality assessment, and advancing human health diagnostics.

Numerous efforts have been laid in the research and development of desired NH₃ sensors based on semiconductor metal oxides, ^{8,9} conducting polymers, ¹⁰ and metal—organic frameworks (MOFs), ¹¹ owing to their desirable properties such as high sensitivity, low cost, easy fabrication, flexibility, high surface area, and tunable electronic properties. Nevertheless, metal oxides lack selectivity in complex environments and operate at higher temperatures, conducting polymers degrade over time, affecting reliability, and MOFs face scalability challenges, limiting their overall performance in

Received: May 21, 2024 Revised: August 1, 2024 Accepted: August 19, 2024 Published: August 22, 2024





commercial sensor applications. 12-16 External factors such as adsorbed oxygen in ambient atmosphere and humidity can significantly influence the sensor performance. Moreover, a common challenge across these sensor types is their diminished sensing response upon exposure to high relative humidity (RH) levels. The reduced sensing response is ascribed to the interference of water molecules, which disrupt the interactions between the target gas and the sensing material.¹⁷ To address these challenges, recent advancements in the field of sensor technology have focused on twodimensional (2D) transition metal dichalcogenides (TMDs) like MoS₂, WS₂, WSe₂, and MoSe₂ as promising candidates for NH₃ sensors operating in highly humid environments.^{8,18} These materials possess significant bandgaps, endowing them with unique tunable layer-dependent electronic, optical, thermal, and physiochemical properties. Furthermore, their inherently large surface-to-volume ratio and high charge carrier mobility make them suitable sensing materials for sensor applications. $^{19-21}$ Notably, rhenium disulfide (ReS₂) has attracted significant research attention due to its fixed direct bandgap (1.5-1.6 eV) from bulk to monolayer without indirect-to-direct bandgap transitions. These distinctive characteristics of ReS2 can be attributed to its stable distorted 1T phase and anisotropic crystalline structure with relatively weak interlayer coupling. ^{22,23} The layered configuration of ReS2 offers abundant edge-exposed sites for gas adsorption and facilitates rapid charge transportation during gas adsorption and desorption processes, thereby enhancing its gas sensing properties. 19,24,25 Similarly, Yang et al. reported the fabrication of humidity sensors based on vertically oriented arrays of ReS2 nanosheets, showing rapid adsorption/desorption of water molecules. ²⁶ Despite these favorable attributes and operability in humid environments, the restacking and agglomeration of 2D ReS₂ during gas adsorption and desorption processes result in diminished overall surface area and active sites, thereby compromising sensitivity and selectivity toward target gases at

To address these challenges, the formation of heterostructures of ReS2 with other 2D materials emerges as a promising approach. The direct bandgap of ReS2 enables the formation of stable junctions with 2D materials, while van der Waals interactions between the 2D/2D heterostructures facilitate a synergistic interplay, mitigating the lattice mismatch issues encountered in semiconductor heterostructures. 27,28 This synergy gives rise to intriguing physical phenomena, including ultrafast charge separation, distinctive interlayer coupling, and customizable band alignments, beneficial toward improving sensitivity in ${\rm ReS_2}$ -based gas sensors. 19,29,30 Toward this approach, MXenes, a versatile family of 2D transition metal carbides, nitrides, and carbonitrides, have emerged as a promising candidate in sensor applications, as summarized in Table S1. MXenes exhibit exceptional properties, including mechanical flexibility, high electrical conductivity, large surface area, strong hydrophilicity, and tunable surface chemistry.^{31,32} The accordion-like delaminated layers of MXene $(Ti_3C_2T_x)$ sheets exhibit a large surface area and excellent electrical conductivity, facilitating easy charge carrier transportation during the sensing process and improving the gas sensing characteristics. In addition to these properties, the hydrophilic characteristics and atomic defect formation in Ti₃C₂T_x significantly contribute to nucleation sites, which are responsible for the oxidative degradation of Ti₃C₂T_x. The surface terminal groups (oxide and hydroxide) actively

participate in the oxidation process of $Ti_3C_2T_x$ by breaking the Ti-C bonds to form Ti-O bonds, resulting in the alteration of large surface area and electrical properties.³⁴

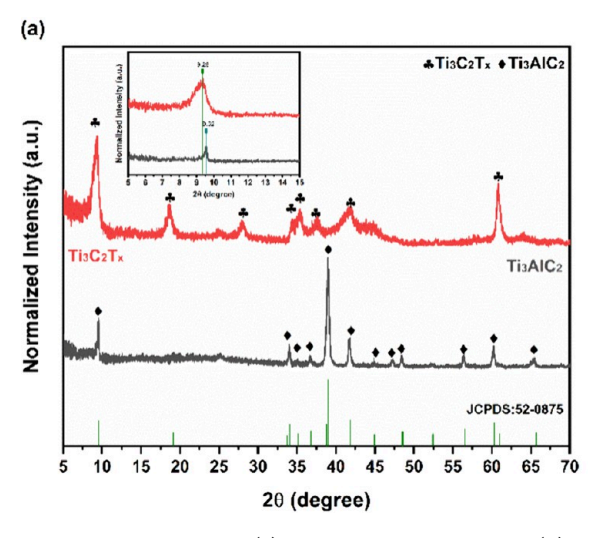
First principle density functional theory (DFT) calculations showed that the adsorption energy and charge transfer of ReS2 and $Ti_3C_2T_x$ toward NH₃ were -0.19 eV and -0.04 and -0.36eV and -0.098, respectively. 35,36 The surface terminal groups of Ti₃C₂T_x help to modulate the work function between ReS₂ and Ti₃C₂T_x, facilitating an easy electron exchange between the materials and generating additional active sites for NH3 gas molecules. This results in an increased charge transfer value and adsorption energy at the interface. Similar results were reported by Tian and co-workers for Ti₃C₂T_x/MoS₂ heterostructures, indicating enhanced adsorption energy and charge transfer value toward NH3 in comparison to pristine $Ti_3C_2T_x$ and MoS_2 .³⁷ The heterostructure formation modulates changes in the electrical properties and enhances the gas sensitivity. Furthermore, Liu et al. reported 5-fold and 12-fold increases in adsorption energy and charge transfer, respectively, after the synthesis of Ti₃C₂T_x composites.³⁸ Hence, the interface engineering of ReS₂ and Ti₃C₂T_x would enhance the surface area, stability, and conductivity of their heterostructures, thereby improving the NH₃ sensing performance under high humidity conditions.

In previous reports, ReS2 or its composites were prepared using the CVD method, which results in bulk properties of ReS₂ and uneven growth.²⁹ The present work focuses on the uniform growth of ReS2 nanosheets on the surface of Ti3C2Tx through a simple and facile hydrothermal method. The growth of 1T stable and edge-exposed ReS₂ nanosheets on the surface of Ti₃C₂T_x prevents the restacking of ReS₂ and oxidation of $Ti_3C_2T_x$. The large surface area of conducting $Ti_3C_2T_x$ acts as a template for ReS₂ nanosheets, generating more interfacial sites for ammonia gas adsorption. The synergistic effect owed to combining ReS₂ nanosheets and conducting Ti₃C₂T_x leads to enhancement of the NH₃ sensing response ranging from 7.8 to 12.4% over a relatively high humidity range of 15-85% at room temperature, exhibiting fast response and fast recovery time. Additionally, the gas sensing investigations performed in ambient conditions demonstrate remarkable reversibility and stability in the gas sensing curves, indicating the potential of ReS₂/Ti₃C₂T_x-based sensors as a cost-effective solution for NH₃ monitoring in a high-humidity environment.

EXPERIMENTAL SECTION

Chemicals. The chemicals in the present study were used as received without any further purification; MAX (Ti₃AlC₂, ≥90%, Sigma-Aldrich), lithium fluoride (LiF, Sigma-Aldrich), hydrochloric acid (HCl, 37%, Fisher), dimethyl sulfoxide (C₂H₆OS, 99.9%, Fisher), ammonium perrhenate (NH4ReO4, 99%, Fisher), hydroxylamine hydrochloride (HONH2·HCl, 99%, Acros Organics), and thiourea (SC(NH₂)₂, 99%, Fisher) were used for materials synthesis. For the analysis of gas sensing properties, a range of test gases were utilized, including ethanol (C₂H₆O, 99.5%, Sigma-Aldrich), methanol (CH₃OH, 99.8%, Fisher), 1-propanol (CH₃CH₂CH₂OH, 99%, Alfa Aesar), ammonium hydroxide (NH₄OH, 30-33% in H₂O, Sigma-Aldrich), formaldehyde (CH₂O, 37% in H₂O and stabilized with ~5-15% methanol, Fisher), xylene (C₆H₄(CH₃)₂, 98%, Acros Organics), N,N-dimethylformamide (HCON(CH₃)₂, 99.8%, Sigma-Aldrich), toluene (C₆H₅CH₃, 99.5%, Fisher), and acetone ((CH₃)₂CO, 99.5%, Fisher). A conductive silver paint procured from Ted Pella was used for the gas sensor electrodes in this study.

Synthesis of $Ti_3C_2T_x$, ReS_2 , and Their Heterostructures. Synthesis of $Ti_3C_2T_x$ from the Ti_3AlC_2 phase used the chemical etching method according to published methods.³⁹ In a typical



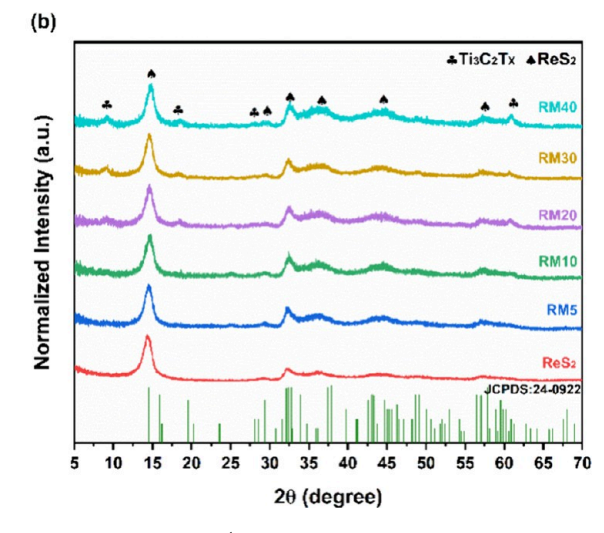


Figure 1. Diffraction pattern of (a) Ti₃AlC₂ and Ti₃C₂T_x and (b) ReS₂ and its heterostructures (RM5, RM10, RM20, RM30, and RM40).

experiment, LiF (1.6 g, 61.7 mmol) was first dissolved in 11 mL of HCl (9M), and the entire mixture was added to 40 mL of nanopure water and magnetically stirred for 30 min to get a homogeneous mixture. Subsequently, Ti₃AlC₂ (500 mg) was slowly added to the above prepared solution followed by magnetic stirring for 24 h at room temperature. The obtained product was subjected to multiple washes with nanopure water and ethanol through centrifugation at 3500 rpm to ensure that all acid was removed (achieve a pH \sim 7). After washing, the precipitates were magnetically stirred with dimethyl sulfoxide (DMSO) (0.5 mg/mL) for 2 h to facilitate intercalation of $Ti_3C_2T_x$ sheets and delamination of the $Ti_3C_2T_x$ sheets. The product was then repeatedly washed with nanopure water and ethanol through centrifugation at 6000 rpm to remove DMSO, followed by bath and probe sonication in ethanol for 2 h in an ice bath. The final product exfoliated Ti₃C₂T_x sheets—were freeze-dried and stored under vacuum for further use.

ReS₂ chrysanthemum-like microspheres were synthesized using the one-pot hydrothermal method. Typically, NH₄ReO₄ (0.322 g, 1.2 mmol) and HONH2·HCl (0.125 g, 1.8 mmol) were magnetically stirred in 40 mL of nanopure water to obtain a transparent solution. Subsequently, $SC(NH_2)_2$ (0.206 g, 2.7 mmol) was added to the above solution, and the mixture was magnetically stirred for 1 h. Then, for synthesizing ReS₂/Ti₃C₂T_x heterostructures, various amounts of $Ti_3C_2T_x$ (0, 7.5, 15, 30, 45, and 60 mg) were magnetically stirred for 30 min in the aforementioned solution. The prepared solutions of ReS_2 with and without $Ti_3C_2T_x$ (in predetermined quantities) were then loaded in a 100 mL Teflon-lined stainless-steel autoclave and treated at 220 °C for 24 h. After cooling to room temperature (RT), the obtained precipitates were washed three times with nanopure water through centrifugation at 6000 rpm and dried in a vacuum oven overnight. The dried samples were labeled as ReS_2 (without $Ti_3C_2T_r$), RM5 (7.5 mg $Ti_3C_2T_x$), RM10 (15 mg $Ti_3C_2T_x$), RM20 (30 mg $Ti_3C_2T_x$), RM30 (45 mg $Ti_3C_2T_x$), and RM40 (60 mg $Ti_3C_2T_x$).

Materials Characterization. The phase and morphology of $Ti_3C_2T_x$, ReS_2 , and $ReS_2/Ti_3C_2T_x$ were examined using a Rigaku MiniFlex600 diffractometer with Cu K_α radiation ($\lambda=1.54056$ Å), JEOL/JSM-F100 Schottky field emission scanning electron microscope equipped with energy dispersive X-ray analysis (EDAX), and JEOL-2100Plus transmission electron microscope. The X-ray photoelectron spectroscopy (XPS) analyses of the synthesized samples were carried out to investigate the surface chemistry and chemical composition using an Escalab 250Xi XPS system (Thermo Fisher Scientific) equipped with monochromatized Al K-alpha radiation at hv=1486.6 eV for XPS at the Advanced Materials Processing and Analysis Centre, University of Central Florida. Surface charge analysis was conducted with a Litesizer DLS 500 particle analyzer (Anton Paar). The Raman spectra were recorded using a confocal Raman microscope (WITec alpha300R) spectrometer with a 532 nm

wavelength laser. The Brunauer–Emmett–Teller (BET) technique was used to estimate the specific surface area and analyze the physical adsorption of gas molecules using Quantachrome/NOVAtouch LX-2.

Sensor Fabrication. Alumina substrates (2 × 2 cm) were used as a sensor substrate. Silver paste (Ted Pella) was meticulously brushpainted onto the alumina substrate, ensuring 1 mm separation to create two silver electrodes. Meanwhile, the synthesized ${\rm Ti}_3{\rm C}_2{\rm T}_x$, ${\rm ReS}_2$, and ${\rm ReS}_2/{\rm Ti}_3{\rm C}_2{\rm T}_x$ heterostructures were dispersed in isopropanol (10 mg/mL) and subjected to sonication for 10 min each. Subsequently, the sonicated solution was drop-cast (40 $\mu{\rm L}$) on silver-deposited alumina substrates for fabricating the gas sensors, as shown in Figure S1.

Gas Sensing Setup and Characterization. To investigate the gas sensing properties of synthesized materials, a custom-built 10 L measurement setup was used. This sensing setup was equipped with a sample holder, a heater, and a gas mixing fan. Prior to the initiation of the gas sensing measurements, the sensing chamber was preheated at 200 °C for 30 min and an exhaust fan was used to eliminate undesired gases from the chamber. After cooling to room temperature (RT), the fabricated sensors were placed inside the sensing chamber and connected to the Keithley 2401 source meter using two-probe connections. The fabricated sensors were then tested in different analyte gases, including ethanol, methanol, propanol, xylene, toluene, formaldehyde, ammonia, dimethylformamide, and acetone. Different amounts of these liquids were injected onto a heater placed inside the sensing chamber using the Hamilton microliter syringe (Hamilton Bonaduz AG, Switzerland), resulting in the generation of different concentrations of analyte gases. The concentration of different analyte gases was calculated using eq 1:

$$C = 22.4 \frac{\rho T V_{\rm s}}{273MV} \times 100 \tag{1}$$

where C is the concentration of the injected analyte, 22.4 is the constant representing 1 mole of gas at standard temperature and pressure, ρ is the density of the liquid, T is the testing sensor temperature, V_s is the amount of liquid inserted, M is the molecular weight of the injecting liquid, and V is the volume of the chamber.

The changes in resistance were recorded by applying a 1 V DC potential across the two-terminal connection of the sensor in the absence and presence of different analyte gases. The sensor response for the change in resistance was calculated using eq 2

$$S = \left(\frac{\left|R_{\rm a} - R_{\rm g}\right|}{R_{\rm a}}\right) \times 100\tag{2}$$

where R_a and R_g denote the sensor resistances in air and analyte gas, respectively. Response and recovery times were determined by

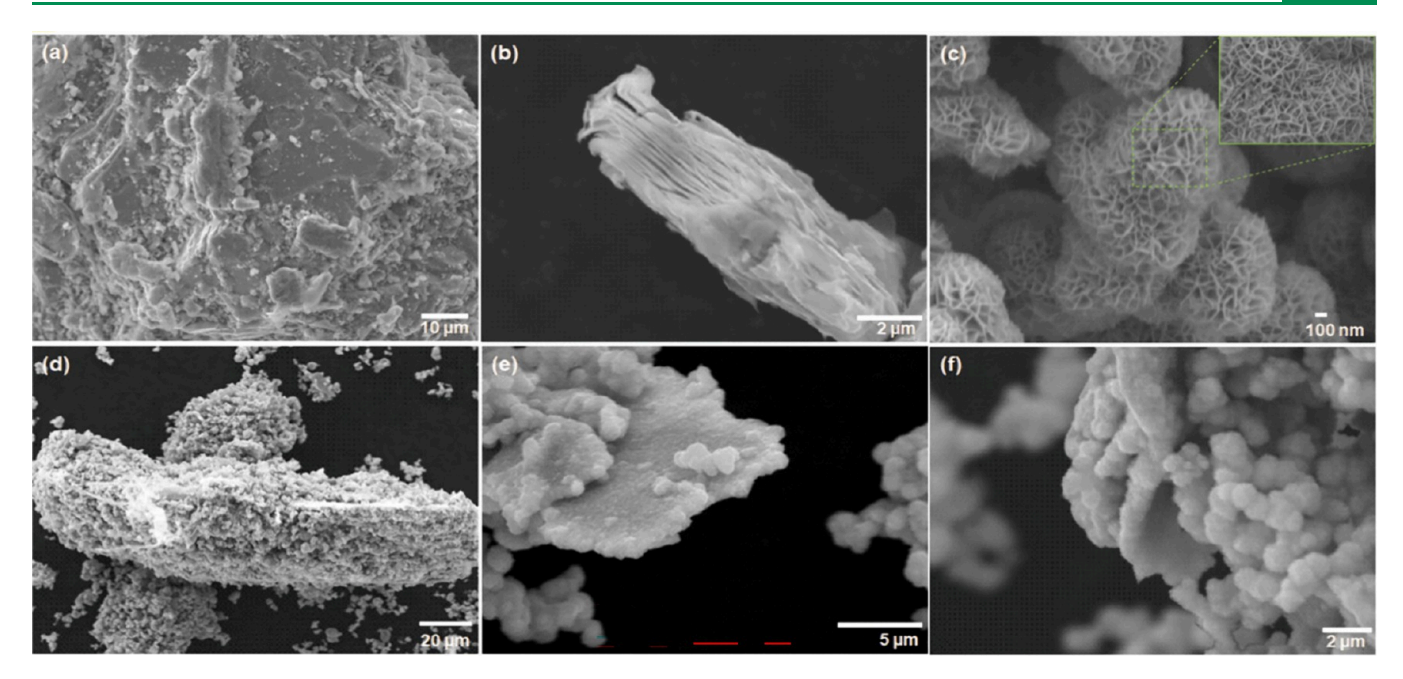


Figure 2. FESEM micrographs of (a) Ti_3AlC_2 , (b) $Ti_3C_2T_{xy}$ (c) ReS_2 (inset: magnified view), and (d-f) RM30 heterostructure at different magnifications.

saturating the response and recovery curves to 90%. Additionally, a humidifier and dehumidifier were also connected to the sensing chamber to record the different humidity concentrations with and without the analyte gases. At a specific concentration of the analyte gas, the fluctuation in the relative humidity (RH) remained within $\pm 5\%$ before and after the sensing measurement. The RH values were monitored using a digital hygrometer kept within the sensing chamber.

RESULTS AND DISCUSSION

Note: Sensor performance analysis revealed that the RM30-based sensor showed optimal results, and therefore, several characterization techniques were employed primarily to characterize this material.

Structural, Morphological, and Optical Investigations of Ti₃C₂T_x, ReS₂, and Their Heterostructures. X-ray diffraction (XRD) analysis was performed to validate the crystal structures of Ti₃AlC₂, Ti₃C₂T_x, ReS₂, and their heterostructures (Figure 1). The diffraction pattern of Ti₃AlC₂ (Figure 1a) exhibited distinct peaks at 9.56, 34.02, 36.71, 38.96, 41.70, 48.43, 56.38, and 60.22°, corresponding to (002), (101), (103), (008), (105), (107), (109), and (110) lattice planes, respectively, consistent with JCPDS card no. 52-0875. 42,43 After the chemical etching treatment on Ti₃AlC₂, the disappearance of the peak at $\sim 39^{\circ}$ in the $Ti_3C_2T_x$ spectrum indicated the selective removal of aluminum from Ti₃AlC₂, confirming the formation of the hexagonal phase of $Ti_3C_2T_x$. Moreover, the diffraction peaks at 9.08 and 18.37° corresponding to (002) and (004) planes were attributed to the -F terminal group, while the peaks at 27.84, 37.45, 41.59, and 60.57° corresponding to (006), (103), (105), and (110) planes were associated with the -OH terminal group of $Ti_3C_2T_{x^*}^{46}$ It is evident that the surface terminal groups (-F and -OH) of $Ti_3C_2T_x$ arise after the chemical etching of Ti₃AlC₂. Furthermore, the intercalation and delamination processes induced a shift in the Ti₃AlC₂ peak at 9.56° to a lower Braggs angle, 9.08° (inset of Figure 1a),

indicative of an increased interlayer spacing in the ${\rm Ti}_3 {\rm C}_2 {\rm T}_x$ sheets. 47

Furthermore, the XRD pattern of ReS₂ nanosheets confirm their triclinic phase, as indicated by distinct peaks observed at 14.28, 29.08, 32.34, 36.08, 48.93, and 57.21°, assigned to the (001), (002), (020), (111), (202), and (-420) planes, respectively, consistent with JCPDS card no. 24-0922 (Figure 1b).²⁹ The absence of intense peaks signifies the presence of a disordered 1T layered structure of ReS₂. 48,49 The XRD pattern of ReS₂/Ti₃C₂T_x heterostructures reveals distinct peaks corresponding to both the ReS₂ and Ti₃C₂T_x phases, indicating the successful synthesis of the heterostructures using the onepot hydrothermal method. Notably, the peaks attributed to (002), (004), (006), and (110) planes of $Ti_3C_2T_x$ intensified with an increasing concentration of $Ti_3C_2T_x$ in $ReS_2/Ti_3C_2T_x$ heterostructures. The diffraction patterns of the Ti₃C₂T_x and RM30 samples were analyzed over a period of 90 days upon exposure to NH3 gas under high humidity conditions, as shown in Figure S2. The diffraction pattern of $Ti_3C_2T_x$ exhibits significant shifts in its prominent peak at $\sim 9^{\circ}$ and the emergence of another peak around ~25°, indicating the presence of anatase TiO₂ (Figure S2a).⁵⁰ The appearance of the anatase TiO_2 peak arises due to the oxidation of $Ti_3C_2T_x$ in the ambient environment. In RM30, there is no significant change in the diffraction pattern, indicating distinct peaks of the ReS₂ and Ti₃C₂T_x phases as shown in Figure S2b.

The morphologies of Ti_3AlC_2 , $Ti_3C_2T_x$, ReS_2 , and their corresponding heterostructures were investigated by scanning electron microscopy (SEM), as illustrated in Figure 2. The SEM micrographs of Ti_3AlC_2 and $Ti_3C_2T_x$ are shown in Figure 2a,b. Ti_3AlC_2 displays a rock-like morphology (Figure 2a), while the selective etching of Al in Ti_3AlC_2 reveals multilayered exfoliated sheets of $Ti_3C_2T_x$ with an average interlayer spacing of \sim 73 nm (Figure 2b). The ReS_2 micrograph showed a 3D chrysanthemum-like uniform microsphere morphology, comprising curly and vertically oriented layered nanosheets (Figure 2c). The average thickness and length of ReS_2 nanosheets were approximately \sim 7 and \sim 245 nm, respectively (inset of Figure

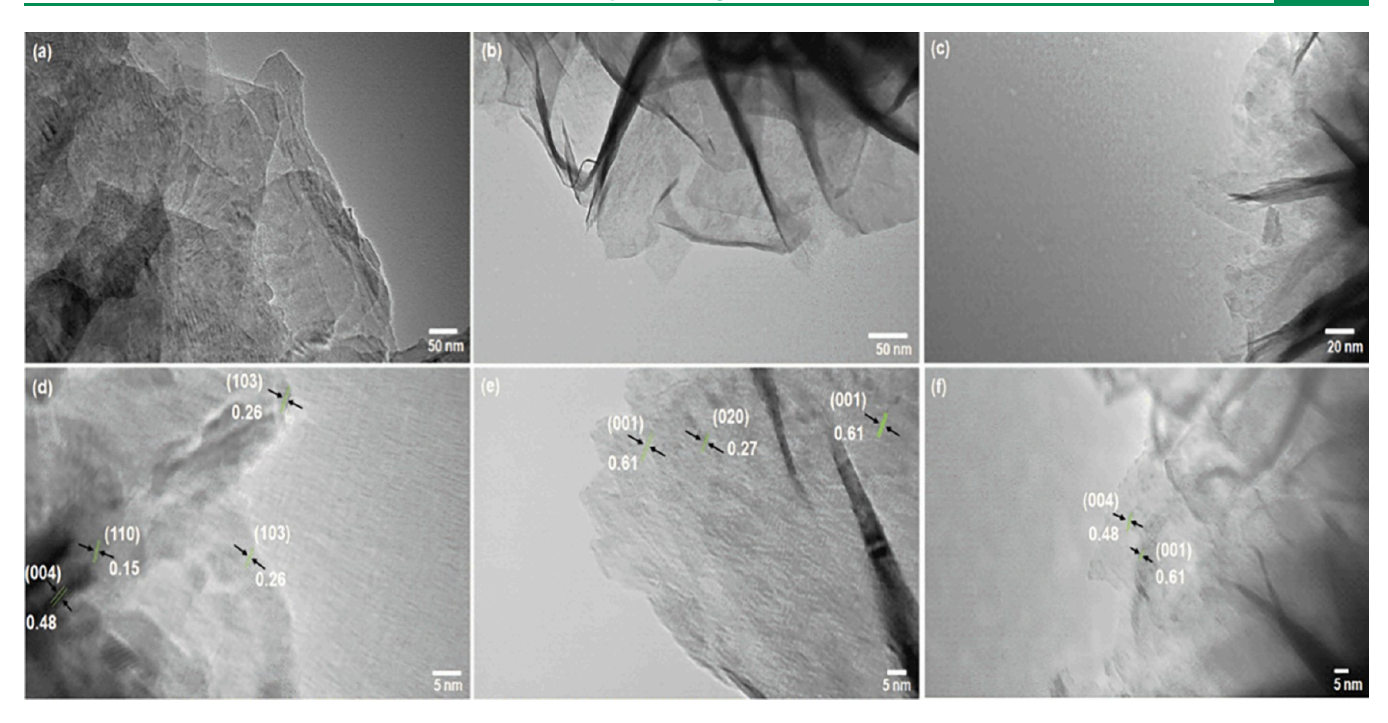


Figure 3. TEM and HRTEM micrographs of (a, d) Ti₃C₂T_{xy} (b, e) ReS₂, and (c, f) the RM30 heterostructure.

2c). Figure 2d-f and Figure S3 present SEM micrographs of RM heterostructures, illustrating ReS₂ nanosheets uniformly grown on the surface and edges of Ti₃C₂T_x sheets. Dur to their large surface, the Ti₃C₂T_x sheets serve as a scaffold for ReS₂ nanosheet deposition. At higher magnification (Figure 2f), the average length of ReS₂ nanosheets was ~100-150 nm, indicating a reduction in length after introducing Ti₃C₂T_x sheets. The resulting morphology of RM heterostructures avoids the restacking and agglomeration of ReS2, consequently increasing their edge-adsorption sites and facilitating the formation of an enhanced surface area for the adsorption of gas molecules. Field emission SEM (FESEM) micrographs of Ti₃C₂T_x and RM30 samples were collected over a period of 90 days upon exposure to NH3 gas under high humidity conditions, as shown in Figure S4. Small blisters were observed on the surface and edges of the $Ti_3C_2T_x$ sheets after 30 days of exposure to NH₃. These blisters may have formed due to oxide bonding with Ti atoms to generate TiO2, which is consistent with the XRD data. After 90 days of exposure to NH3 under high humidity, significant oxidation of Ti₃C₂T_x was evident. In contrast, the RM30 micrographs revealed that the edgeexposed ReS₂ nanosheets on the surface of Ti₃C₂T_x remained consistent after 90 days of NH3 exposure at high humidity and room temperature (Figure S5).

Additionally, the elemental composition of ${\rm Ti_3C_2T_{xy}}$ ReS₂, and their heterostructures was examined by using energy dispersive X-ray analysis (EDS) and elemental mapping, as illustrated in Figure S6. In Figure S6a,b, the EDS spectrum and elemental mapping of ${\rm Ti_3AlC_2}$ and ${\rm Ti_3C_2T_x}$ demonstrate the homogeneous distribution of Al, Ti, and C and Ti, C, O, and F within their respective micrographs, respectively. In the case of ReS₂ nanosheets, the mapping analysis reveals a consistent distribution of Re and S elements, maintaining an S/Re ratio of 2:1 (Figure S6c). Remarkably, in the RM heterostructures, both R and S elements were uniformly distributed on ${\rm Ti_3C_2T_x}$ sheets, as depicted in Figure S6d—h.

Transmission electron microscopy (TEM) and highresolution TEM (HRTEM) analyses were conducted to investigate the morphological and crystal structures of Ti₃C₂T_x, ReS₂, and the RM30 heterostructure. Figure 3a,b illustrates that the TEM micrograph highlights distinct features of exfoliated multilayered and curly sheet-like morphologies for $Ti_3C_2T_x$ and ReS_2 , respectively. The ReS_2 nanosheets exhibited an average thickness of ~5 nm, consistent with the FESEM micrograph (Figure 2c). Furthermore, the presence of ultrathin curly ReS₂ nanosheets on the surface of Ti₃C₂T_x sheets was observed in the RM30 heterostructure, as shown in Figure 3c. High-resolution TEM analysis provides insights into the atomic arrangement, with lattice spacing measurements of 0.15, 0.26, and 0.48 nm corresponding to the (110), (103), and (004) planes in Ti₃C₂T_x, respectively, consistent with XRD results (Figure 3d). Similarly, HRTEM micrographs reveal lattice spacings of 0.27 and 0.61 nm, attributed to the (020) and (001) lattice planes of ReS₂, respectively (Figure 3e). In the RM heterostructure, lattice spacings of 0.48 and 0.61 nm align with the (004) and (001) lattice planes of Ti₃C₂T_x and ReS₂, respectively, indicating robust contact between ReS_2 nanosheets with $Ti_3C_2T_x$ in the RM30 heterostructure, as shown in Figure 3f.

X-ray photoelectron spectroscopy was performed to investigate the surface chemistry and chemical composition of the RM30 (ReS₂/Ti₃C₂T_x) heterostructure. The survey spectra of the RM30 heterostructure (Figure 4a) show the signals of Re, S, O, C, and F elements. The peaks at binding energy values of 42, 262/275, and 448 eV are assigned to Re 4f, Re 4d, and Re 4p, while peaks at 162 and 227 eV correspond to S 2p and S2s, respectively, of ReS₂. Furthermore, the peaks at 284.6, 531, and 684.5 eV are associated with C 1s, O 1s, and F 1s, respectively. The corelevel spectrum of Re 4f (Figure 4b) exhibits two spin—orbit coupled energy states, $4f_{7/2}$ and $4f_{5/2}$, at 41.75 and 44.15 eV, respectively, indicating the presence of the Re⁴⁺ oxidation state in the 1T-phase structure of ReS₂. Similarly, the S 2p core

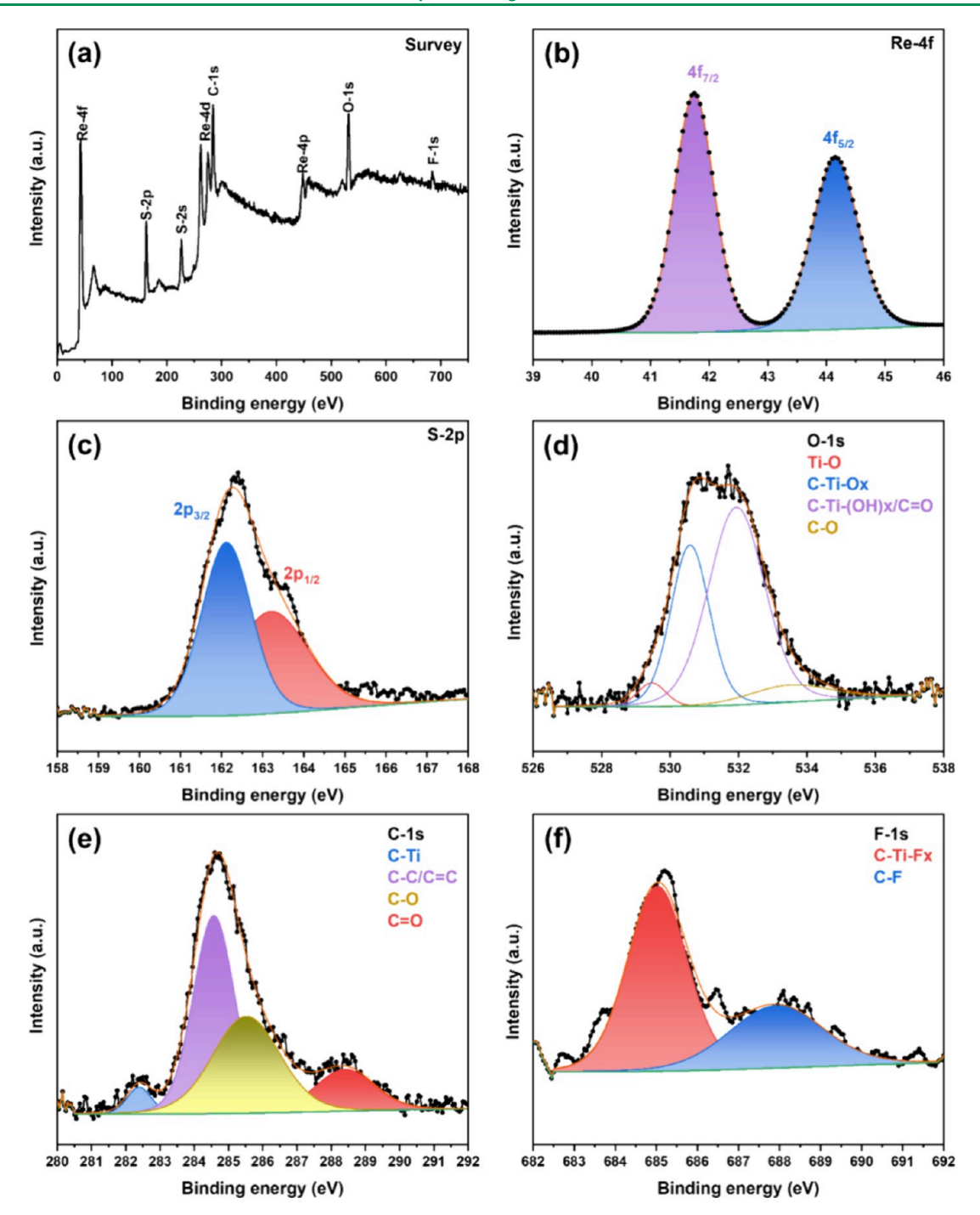
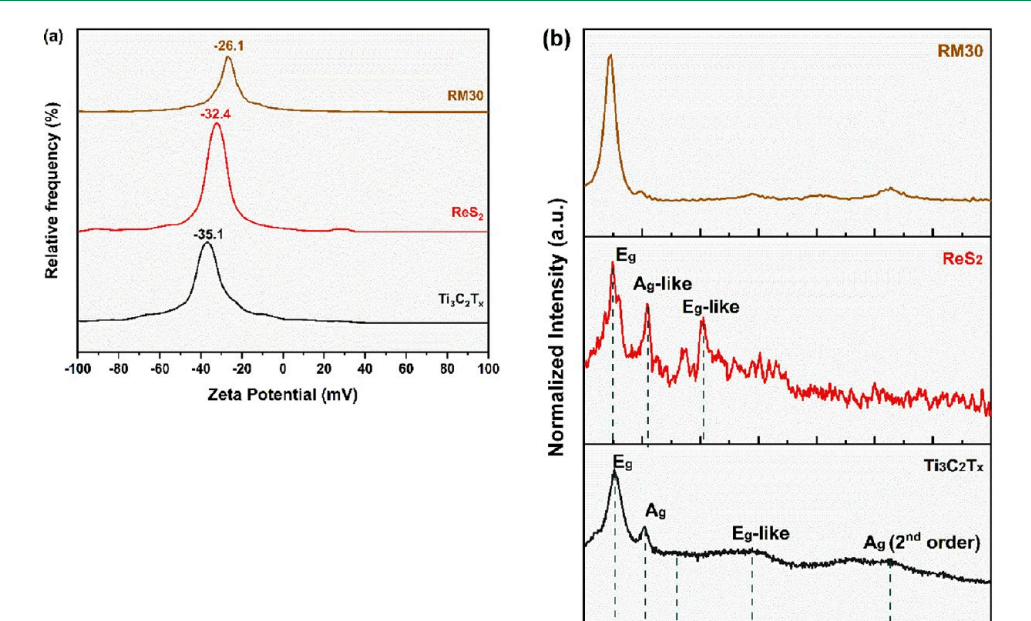


Figure 4. XPS spectra of the RM30 heterostructure: (a) full survey, (b) Re 4f core-level spectrum, (c) S 2p core-level spectrum, (d) O 1s core-level spectrum, (e) C 1s core-level spectrum, and (f) F 1s core-level spectrum.

spectrum arises from the $2p_{3/2}$ and $2p_{1/2}$ spin—orbit coupled energy states at 162.15 and 163.2 eV, respectively, corresponding to the S^{2-} bond energy in ReS₂, as shown in Figure 4c.⁵³ In the RM30 heterostructure, no signals were observed for Ti, which could be attributed to the blocking effect of the dense outer layer of ReS₂ nanosheets, as XPS measurements are limited to detecting surface composition.²⁹ The core-level spectrum of O 1s exhibits peaks at 529.45 and 530.6 eV, corresponding to mild oxidation (Ti–O) and O-terminated surface groups (C–Ti–O_x), respectively, after hydrothermal treatment (Figure 4d).^{29,54,55} Furthermore, carbonaceous and hydroxyl groups at 531.95 eV (C–Ti–(OH)_x/C=O) and

533.6 eV (C–O) are present in the O 1s spectrum. ⁵⁴ Figure 4e,f indicates the core-level spectra of C 1s and F 1s arising from $Ti_3C_2T_x$ in heterostructures. The C 1s core-level spectrum shows peaks at 282.4, 284.6, 285.5, and 288.4 eV, indicating the presence of C–Ti, C–C/C=C, C–O, and C=O bond interactions, respectively (Figure 4e). ^{56,57} The F 1s spectrum indicates peaks at 685.1 and 688 eV, corresponding to C–Ti– F_x and C–F bonds, respectively (Figure 4f). ⁵⁸

The survey spectra of the RM30 heterostructure after 90 days indicate similar Re, S, O, C, and F element signals, as shown in Figure S7a. The core-level spectra of Re 4f and S 2p exhibit similar peak positions, as shown in Figure S7b,c.



100

200

400

500

Raman Shift (cm-1)

600

700

Figure 5. (a) Zeta potential and (b) Raman spectra of Ti₃C₂T_x, ReS₂, and the RM30 heterostructure.

However, the O 1s spectrum shows peaks at 530.1, 530, 531.95, and 533.75 eV, corresponding to Ti-O, C-Ti-O_x, C-Ti-(OH)_x/O=C, and C-O bonds, respectively (Figure S7d). The C 1s spectrum shows peaks at 281.9, 284.59, 285.5, and 288.4 eV attributed to C-Ti, C-C, C-O, and C=O bonds, and the F 1s spectrum shows peaks at 684.65 and 690 eV, corresponding to C-Ti-F_x and C-F bonds, respectively, in the RM30 heterostructure after 90 days (Figure S7e,f).

Zeta potential measurements were conducted to understand the surface charges on ReS₂, Ti₃C₂T_x, and the RM30 (ReS₂/ Ti₃C₂T_x) heterostructure, as shown in Figure 5a. ReS₂ nanosheets and Ti₃C₂T_x multilayer sheets exhibited zeta potentials of -32.4 and -35.1 mV, respectively, indicating their highly negative surface charges. Chemical etching of $Ti_3C_2T_x$ results in the formation of -OH, -O, and -F, surface functional groups, consistent with the XPS analysis.⁵⁹ The surface functional groups of Ti₃C₂T_x help modulate the work function of ReS2 nanosheets to form the RM30 heterostructure. 17,60 This interaction can lead to charge redistribution at the interface, resulting in a more stable surface charge and, thus, a lower zeta potential of -26.1 mV. The presence of negative surface charge on the RM30 heterostructure will be beneficial for effective target gas adsorption, promoting selectivity and responsivity.

The vibrational characteristics of ${\rm Ti_3C_2T_{xr}}$ ReS₂, and their heterostructures were systematically examined by using Raman spectroscopy. Figure 5b and Figure S8 illustrate the Raman spectra of all samples, covering the wavelength ranges of 50–700 and 1100–1800 nm, respectively. ${\rm Ti_3C_2T_x}$ revealed distinct peaks corresponding to the $E_{\rm g}$ (in-plane) and $A_{\rm 1g}$ (out-of-plane) Raman active mode within the range of 50–700 cm^{-1.61} Specifically, the Raman peak at 151.8 cm⁻¹ was attributed to the $E_{\rm g}$ Ti–C vibrations, ⁶² while the peaks at 203.3 and 254.4 cm⁻¹ were associated with mixed out-of-plane vibrations involving Ti–C and H atoms of ${\rm Ti_3C_2(OH)}$. ^{63,64} Additionally, peaks at 398.5 and 626.8 cm⁻¹ were linked to inplane vibration of O atoms and second-order out-of-plane Ti–

C vibrations, respectively.⁶⁵ Within the Ti₃C₂T_x structure, peaks at 1372.3 and 1556.2 cm⁻¹ corresponded to the disordered (D band) and ordered sp² (G band) carbon atoms, respectively.⁶⁶ The calculated intensity ratio of $I_{\rm D}/I_{\rm G}$ (0.97) suggested the presence of amorphous carbon in Ti₃C₂T_x. 67 ReS₂ exhibited Raman peaks at 160.6 and 209.5 cm⁻¹ assigned to in-plane and out-of-plane vibrational modes in Re atoms, respectively, while a peak at 304.9 cm⁻¹ was attributed to the in-plane vibrational mode of S atoms. 40,68 Additional characteristic peaks within the range of 100-400 cm⁻¹ reflected the unique symmetry in the distorted 1T structure of ReS₂.⁶⁹⁻⁷¹ In the case of heterostructures, individual peaks of ReS_2 and $Ti_3C_2T_x$ were observed. The calculated intensity ratios of D and G bands I_D/I_G for the RM10, RM20, RM30, and RM40 heterostructures were found to be 0.94, 0.97, 0.95, and 0.93, respectively, suggesting the noncovalent attachment of ReS₂ nanosheets on Ti₃C₂T_x sheets via van der Waals forces.2

The analysis of the specific surface area and pore size distribution was conducted for $Ti_3C_2T_{x\nu}$ ReS₂, and their heterostructures through nitrogen (N₂) adsorption and desorption isotherms obtained from BET measurements. The N₂ adsorption/desorption isotherms of all the samples exhibited a type-IV behavior and H3 hysteresis loop, indicative of the layered structure in $Ti_3C_2T_x$, ReS_2 , and their heterostructures (Figure S9). Additionally, the hysteresis curve of samples at relative pressures (P/P_0) of 0.4 and 0.9 indicates their mesoporous nature. The calculated specific surface areas (S_{BET}) of the heterostructures were approximately 8 and 1.3 times higher than those of $Ti_3C_2T_x$ (1.6 m² g⁻¹) and ReS_2 (6.94 m² g⁻¹), respectively. The collective analysis of S_{BET} and pore size distribution underscores the synergistic effect of $Ti_3C_2T_x$ and ReS_2 , leading to an increased specific surface area in the heterostructures. This augmentation leads to an increased number of active sites, potentially enhancing gas adsorption and consequently improving sensor response and kinetics.

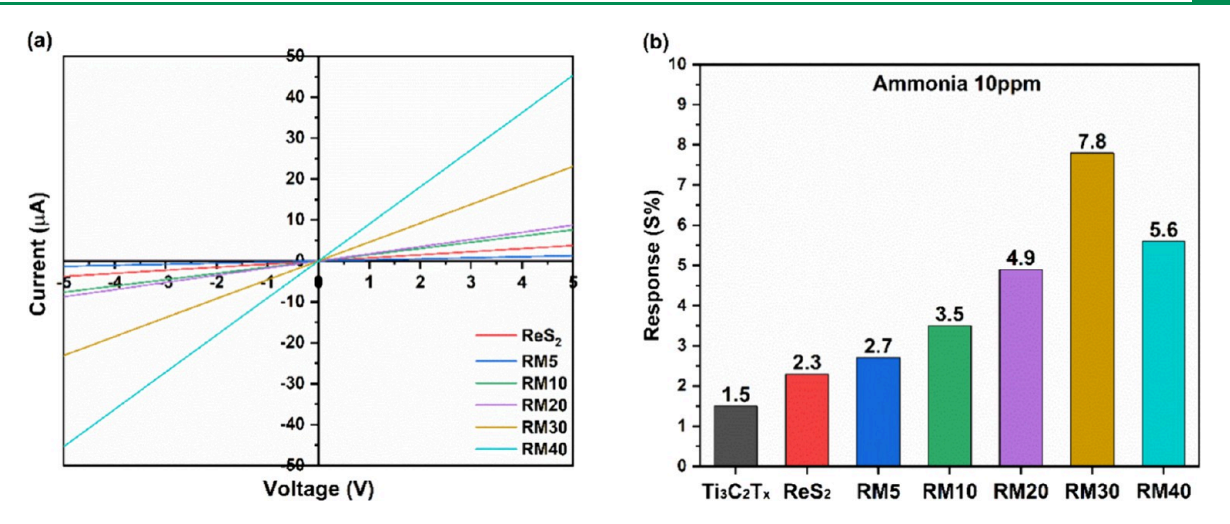


Figure 6. (a) Current–voltage (I-V) characteristics and (b) response histogram to 10 ppm of NH₃ at 15% RH and RT for sensors based on ReS₂, Ti₃C₂T_x, and their heterostructures.

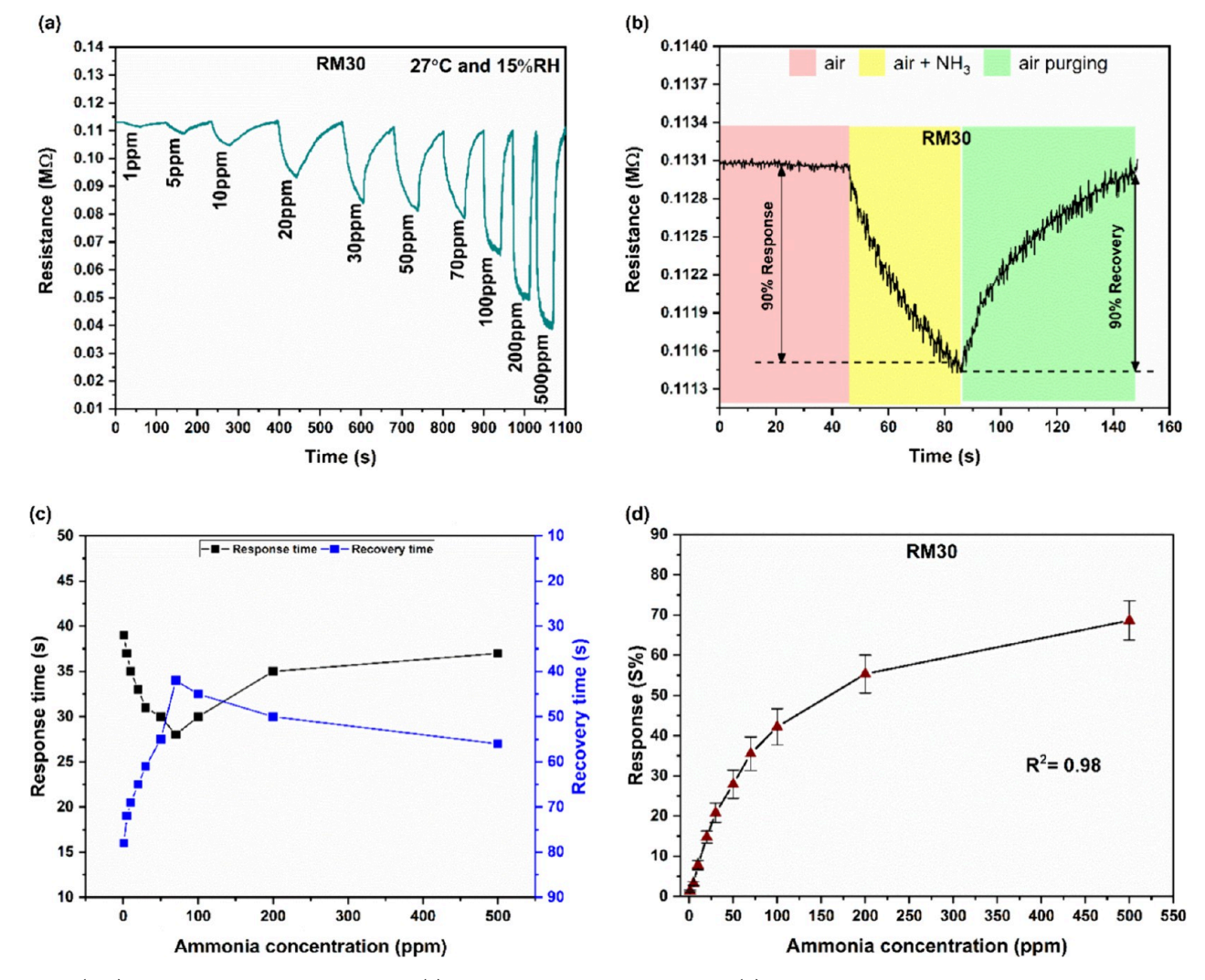


Figure 7. (a, b) Resistance—time transient curves, (c) response and recovery times, and (d) response variation toward 1–500 ppm of NH₃ at 15% RH and RT for the RM30-based sensor.

Insights to Gas Sensing Investigations. To investigate the electrical properties of $Ti_3C_2T_x$, ReS_2 , and their heterostructures, two-terminal current–voltage (I-V) measurements were performed at different voltage ranges (1-5 V),

as depicted in Figure 6a and Figure S10. All the devices show ohmic behavior at RT, and the calculated resistances from the I-V plots of ${\rm Ti}_3{\rm C}_2{\rm T}_x$ and ${\rm ReS}_2$ were 787 Ω and 3.84 ${\rm M}\Omega$, respectively, while the resistances for RM heterostructures start

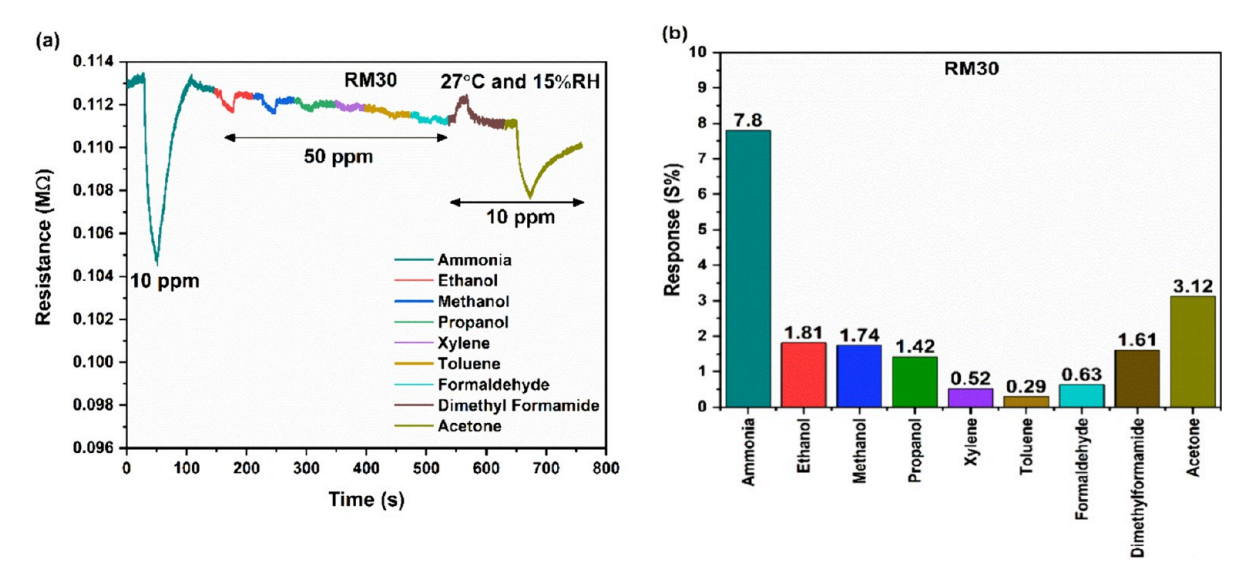


Figure 8. (a) Resistance-time curves and (b) response histogram toward 10 and 50 ppm of different gases at 15% RH and RT.

decreasing from 1.32 to 0.110 M Ω in the voltage range of -5 to 5 V. This indicates that the addition of ${\rm Ti}_3{\rm C}_2{\rm T}_x$ increases the conductivity in RM heterostructures, which helps in improving the charge transportation during the sensing processes.

The gas sensing responses of Ti₃C₂T_x-, ReS₂-, and their heterostructure-based fabricated sensors were investigated on exposure to 10 ppm of NH₃ under 15% relative humidity (RH) and room temperature (27 °C), as depicted in Figure 6b. The sensor response was calculated using eq 2 mentioned in Experimental Section (2.4). The pristine $Ti_3C_2T_x$ (1.5%)- and ReS₂ (2.3%)-based sensors demonstrated a limited response compared to their respective RM heterostructures (RM5 (2.7%), RM10 (3.5%), RM20 (4.9%), RM30 (7.8%), and RM40 (5.6%)) when exposed to 10 ppm of NH₃ at 15% RH and RT. The response histogram illustrates a trend of increasing sensing response for RM5, maximizing at RM30, followed by a decrease for the RM40-based sensor. The increase in the sensor response is ascribed to the synergistic effect of ReS₂ nanosheets grown on the Ti₃C₂T_x surface. The conductive nature and large surface area of Ti₃C₂T_x, coupled with uniformly grown ReS₂ nanosheets, facilitate the trapping of a large number of NH₃ molecules at edge-exposed sites. Conversely, the decrease in sensor response for the RM40 heterostructure is associated with the abundance of surface terminal groups on Ti₃C₂T_{xy} which reduces the availability of active sites for NH₃ adsorption. 47,73 Among the fabricated sensors, the RM30-based sensor exhibited superior sensing performance, indicating the optimal proportion of $Ti_3C_2T_x$ and ReS₂ in heterostructures. Subsequently, further sensing studies were solely conducted on RM30-based sensors.

Figure 7a,b shows the resistance—time transient characteristics of the RM30-based sensor, providing detailed insight into the dynamic changes in resistance as a function of time on exposure to 1–500 ppm of NH₃ at 15% RH and RT. The RM30-based sensor demonstrates a substantial decrease in resistance upon exposure to NH₃, which is characteristic of its n-type semiconductor behavior. Upon purging with air, the sensor promptly returns to its baseline resistance, highlighting its remarkable reversibility, and is observed from the resistance—time curve for 1 ppm of NH₃ (Figure 7b). For comparative analysis, the dynamic resistance—time curves and

response characteristics of ReS₂-based sensors (Figure S11) were also recorded on exposure to 1-500 ppm of NH₃ at 15% RH and RT. Figure 7c represents the effect of the NH₃ concentration on the response time and recovery time of the RM30 sensor. The large and conducting surface of Ti₃C₂T_x with edge-exposed ReS2 nanosheets facilitates efficient charge transportation during NH3 adsorption and desorption, resulting in reduced response/recovery times compared to ReS2-based sensors. Figure 7d illustrates the response characteristics of the RM30-based sensor at different concentrations of NH3. The sensor demonstrates a diverse sensing response, ranging from 1.38 to 68.65%, toward NH₃ concentrations spanning 1-500 ppm at 15% RH and RT. Here, the interaction between NH₃ gas and the sensing surface was evaluated using the Freundlich isotherm model, as expressed by the equation:

$$S\% = A \times C^b \tag{3}$$

where S%, A, C, and b denote the sensor response percentage, a Freundlich constant related to the adsorption capacity, NH_3 concentration, and the Freundlich exponent, respectively. Regression analysis produced a coefficient of determination (R^2) of 0.98, accompanied by distinct parameters (A=4.65) and b=0.45. The high R^2 value suggests a strong correlation between the model and experimental data, affirming that the RM30-based sensor demonstrates a consistent and monotonic response to increasing NH_3 concentrations. This finding establishes a solid foundation for the potential development of a quantitative analysis method employing the $\mathrm{ReS}_2/\mathrm{Ti}_3\mathrm{C}_2\mathrm{T}_x$ heterostructure in NH_3 gas detection applications.

Selectivity is a critical parameter in the realm of gas sensors, particularly in detecting specific gases from complex mixtures. In this context, the selectivity investigation of the RM30-based sensor was conducted on exposure to 10 ppm of NH₃, formaldehyde, and dimethylformamide and 50 ppm of acetone, ethanol, methanol, isopropanol, xylene, and toluene at RT under 15% RH and RT, as depicted in Figure 8a. The sensor resistance decreases upon exposure to reducing gases except for dimethylformamide, which acts as an oxidizing gas. Subsequently, the sensor resistance returns nearly to baseline levels following purging with air. Among the tested analytes, the RM30-based sensor demonstrated a high response toward

ACS Sensors pubs.acs.org/acssensors Article

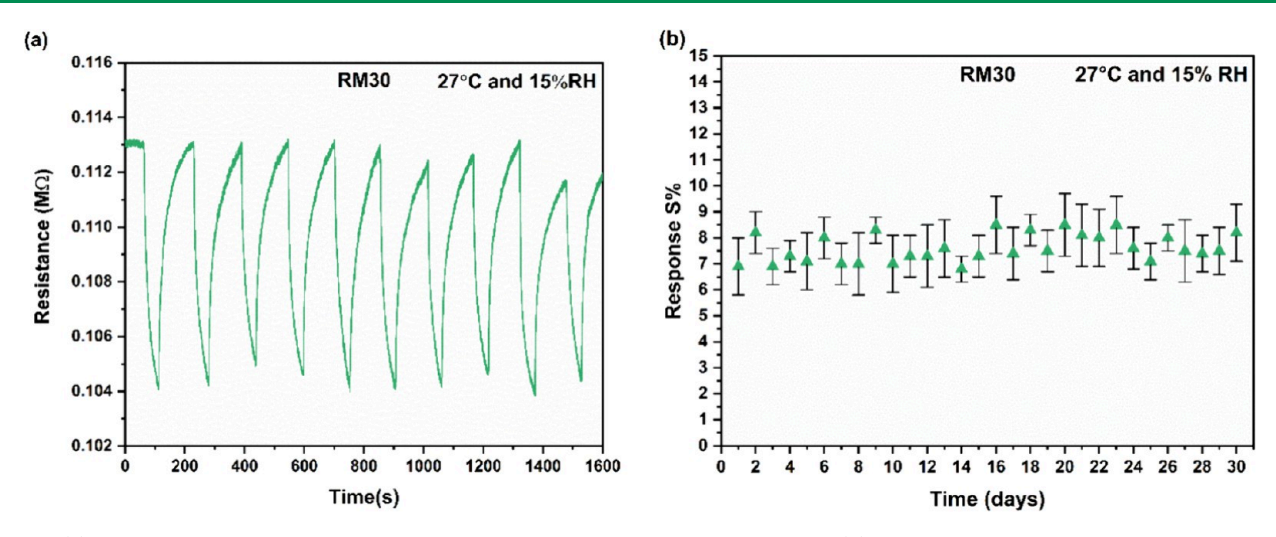


Figure 9. (a) Resistance—time curves for 10 consecutive cycles of the RM30-based sensor and (b) response of five similar RM30-based sensors for 30 days toward 10 ppm of NH₃ at 15% RH and RT (error bars represent the deviation of response from average values calculated from five similar RM30-based sensors).

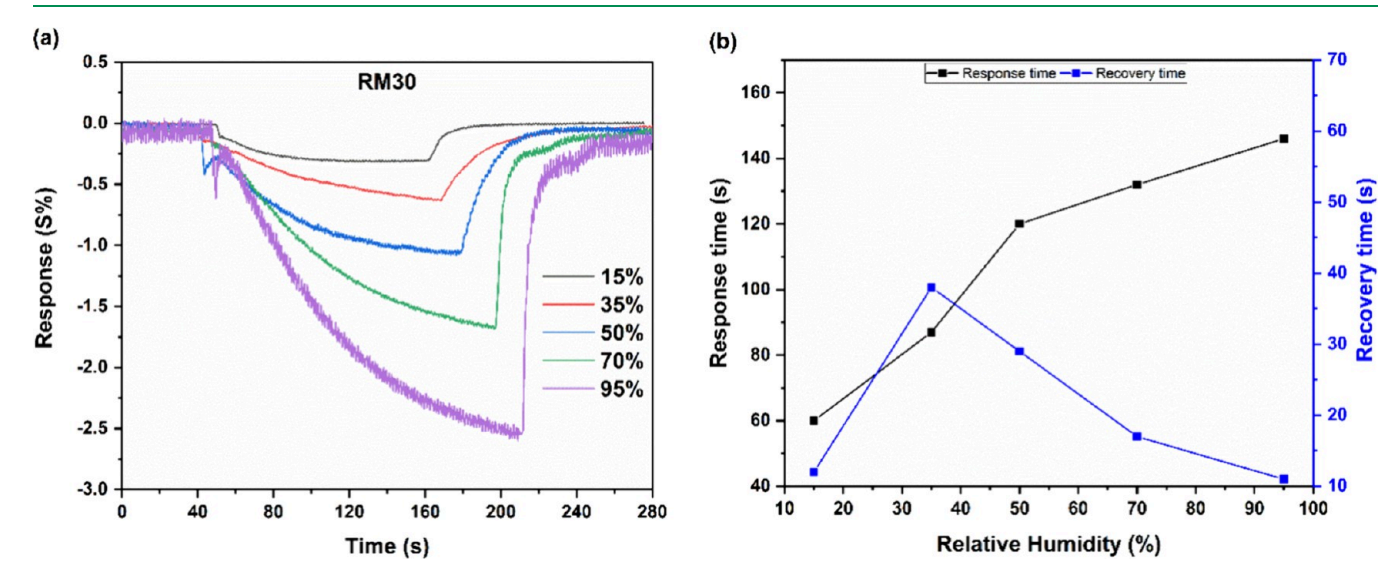


Figure 10. (a) Response–time curves and (b) response and recovery times of the RM30-based sensor toward 15–95% humidity at room temperature.

 $\mathrm{NH_3}$ (7.8%), followed by acetone, ethanol, and methanol. This significant response to $\mathrm{NH_3}$ underscores the exceptional selectivity of the RM30 sensor, as depicted in Figure 8b. Additionally, considering the Knudsen diffusion theory, the diffusion rate of analyte gases can be correlated to their molecular weight. The Knudsen diffusion constant (D_K) is expressed as:

$$D_{\rm K} = \frac{3r}{4} \sqrt{\frac{2RT}{\pi M}} \tag{4}$$

where *r*, *R*, *T*, and *M* are the pore radius, gas constant, temperature, and gas mass, respectively. Hence, the enhanced selectivity toward NH₃ is also partially attributed to the lightweight nature of NH₃ gas as compared to other gases. ⁷⁵

To study the repeatability of the RM30-based sensor, response curves were recorded over 10 consecutive cycles toward 10 ppm of NH₃ at 15% RH and RT, as shown in Figure 9a. Remarkably, no significant differences were observed in the response/recovery curves, indicating excellent repeatability with complete recoverability. Figure 9b illustrates the response

value of five similar RM30-based sensors exposed to 10 ppm of NH $_3$ concentration at 15% RH and RT over 30 days. Importantly, all sensors exhibit robust long-term stability, maintaining response values within a satisfactory range of 7–8.2% with minimal deviation. Additionally, Figure S12a presents the long-term stability of the RM30-based sensor when exposed to 10 ppm of NH $_3$ at 15% RH and room temperature over a period of 90 days, highlighting its practical applicability. The sustained long-term stability of the RM30-based sensor can be attributed to the stable distorted structure of ReS $_2$, which uniformly grows over the surface of Ti $_3$ C $_2$ T $_x$, forming a stable sensing material.

To further elucidate the influence of humidity on the RM30-based sensor, response—time curves were collected across a wide range (15–95%) of humidity levels at ambient room temperature, as depicted in Figure 10a. The RM30 sensor exhibited a decrease in sensor resistance on exposure to different RH values. Notably, the resistance returned to its baseline resistance when the humidity was turned off, suggesting its excellent recoverability. The response and

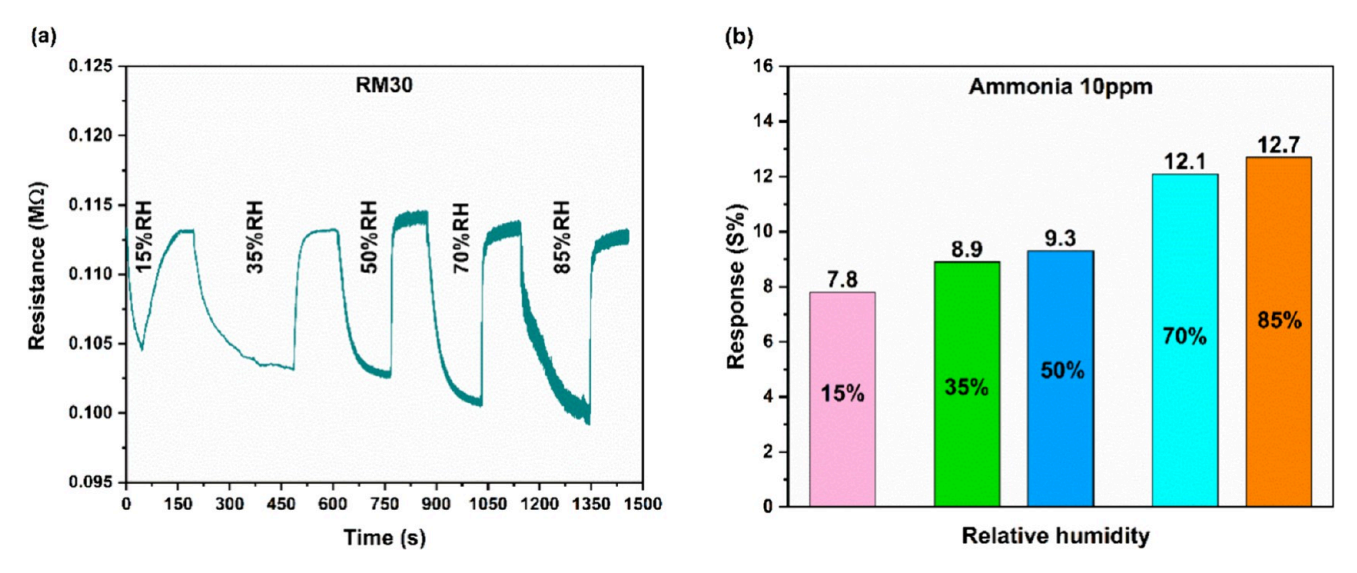


Figure 11. (a) Resistance—time curves and (b) response histogram of the RM30-based sensor to 10 ppm of NH₃ within an RH range of 15–85% and RT.

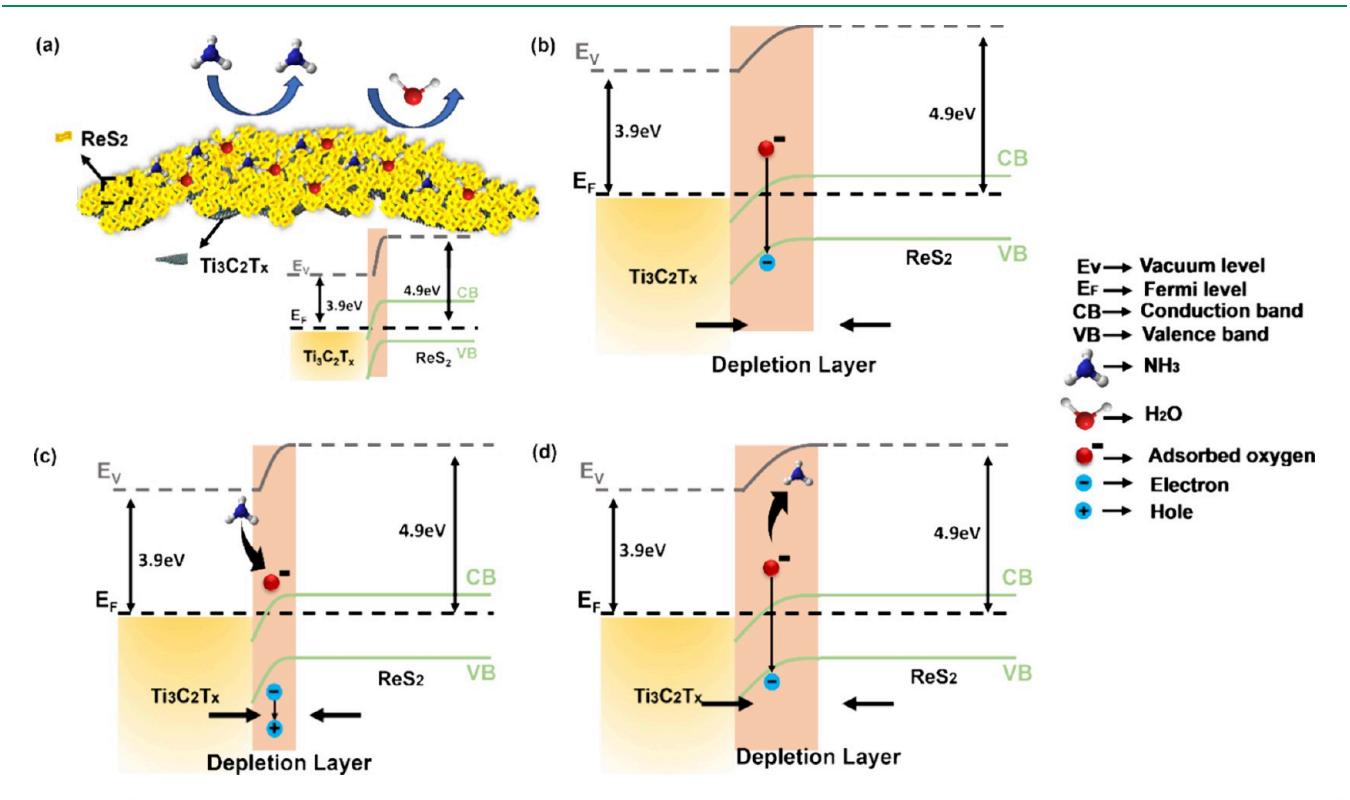


Figure 12. (a) Schematic illustration of the NH₃ gas sensing mechanism on the $ReS_2/Ti_3C_2T_x$ surface along with its energy band structure. (b) Schottky barrier formation of ReS_2 and $Ti_3C_2T_x$ in air and (c, d) in the presence of ammonia.

recovery times of the RM30-based humidity sensor, calculated at varying RH, are depicted in Figure 10b. The response time increases, and the recovery time decreases with increasing humidity levels, indicating the low adsorption and high desorption rates of $\rm H_2O$ molecules on the sensor surface, respectively.

The sensing performance of the RM30-based sensor was also investigated in an environment containing a mixture of NH₃ and H₂O to evaluate its sensing capability under ambient conditions. Figure 11a depicts the resistance—time transient curves of the RM30-based sensor on repeated exposure to 10 ppm of NH₃ at relative humidities ranging from 15 to 85%. It

is observed that the sensor resistance decreases with increasing humidity levels, in agreement with a previous humidity sensing study. The consistent reversibility observed in the sensing curves reflects the robust and durable nature of the sensing material. Additionally, the response histograms in Figure 11b demonstrate an increasing response value ranging from 7.8 to 12.7% across the RH range of 15–85%, emphasizing the sensors' sensitivity to diverse environmental conditions. To further assess long-term stability, $Ti_3C_2T_x$ -, ReS_2 -, and RM30-based sensors were tested toward 10 ppm of NH₃ at 85% RH and room temperature over a period of 90 days, as shown in Figure S12b. The RM30 heterostructure exhibited a minimal

ACS Sensors pubs.acs.org/acssensors Article

change in sensing response (12.4–13%) at 85% RH compared to the $Ti_3C_2T_{x^-}$ and ReS₂-based sensors, indicating the long-term stability of the RM30-based sensor.

Mechanism Visualization for Improved ReS₂/Ti₃C₂T_x Gas Sensing Performance. The classical gas sensing mechanism and energy band structure of the ReS₂/Ti₃C₂T_x (RM30) heterostructure were illustrated to validate the plausible gas sensing characteristics in the present work.⁴⁵ The sensing characteristics are based on the chemical adsorption, oxidation, and desorption processes occurring at the interface between the gas molecule and the sensing material. Structural and morphological analyses reveal the uniform growth of curly, edge-exposed ReS2 nanosheets on the surface of conductive metallic Ti₃C₂T_x, exhibiting a high surface area beneficial for the adsorption of gas molecules (as shown in Figure 12a). The sensing characteristics indicate the n-type behavior of ReS2, which dominates electron transfer after the chemical reaction with NH₃ at the ReS₂/Ti₃C₂T_x interface. The presence of Ti₃C₂T_x facilitates charge transport in the ReS₂/Ti₃C₂T_x heterostructure, confirmed through the I-V characteristics (Figure 6a). In the formation of ReS₂/ Ti₃C₂T_x heterostructures, the lower work function of ReS₂ $(\sim 4.8 \text{ eV})$ facilitates electron injection from higher work function $Ti_3C_2T_r$ (~3.9 eV), establishing an equilibrium Fermi level. 77,78 This electron injection induces band bending in both materials, resulting in the formation of Schottky barriers at the ReS₂/Ti₃C₂T_x interface. The diffusion and drift of electrons lead to the creation of a depletion layer at the ReS₂/Ti₃C₂T_x interface as shown in Figure 12a.79 XPS analysis reveals the participation of atmospheric oxygen below 100 °C in the electron exchange with the surface of the sensing material (zeta potential), forming ionic species through the following reactions (eqs 5 and 6):

$$O_2(gas) \rightarrow O_2(ads)$$
 (5)

$$O_2(ads) + e^- \rightarrow O_2^-(ads)$$
 (6)

The adsorbed oxygen $O_2^-(ads)$ captures electrons from the $ReS_2/Ti_3C_2T_x$ interface, forming an electron depletion layer (EDL) and a hole accumulation layer (HAL) at the interface. The negative surface charges on the $ReS_2/Ti_3C_2T_x$ heterostructure tend to enhance oxygen adsorption, contributing to an increase in the depletion region at the $ReS_2/Ti_3C_2T_x$ interface, as shown in Figure 12b. When exposed to NH_3 under ambient humidity, water molecules react with NH_3 molecules through the following reaction (eq 7):

$$NH_3(gas) + H_2O(ads) \rightarrow NH_4^+(ads) + OH^-$$
 (7)

The adsorbed $\mathrm{NH_4}^+$ subsequently has more free electrons that interact with the adsorbed $\mathrm{O_2}^-$ at the $\mathrm{ReS_2/Ti_3C_2T_x}$ interface through the following chemical reactions (eqs 8 and 9):⁸⁰

$$2NH_4^+(ads) + 3O_2^-(ads) \rightarrow 2NO(ads) + 4H_2O + e^-$$
(8)

$$NO(ads) + \frac{1}{2}O_2(gas) \rightarrow NO_2$$
 (9)

As a result, the electrons captured by the adsorbed oxygen are released back to the HAL, reducing the depletion region and sensor resistance at the $ReS_2/Ti_3C_2T_x$ interface, as illustrated in Figures 7b and 12c. The high surface area of the $ReS_2/Ti_3C_2T_x$ heterostructure provides more adsorption

sites for atmospheric oxygen, which reacts with NH⁴⁺, leading to a higher sensing response. During the purging process, atmospheric oxygen again captures electrons from the $ReS_2/Ti_3C_2T_x$ interface, increasing the sensor resistance and thickness of the depletion region (Figure 12d).

In the context of humidity sensing, the physisorption interaction between water (H_2O) molecules and adsorbed oxygen atoms occurs through the H-bonding at the ReS₂/ $Ti_3C_2T_x$ junction. As humidity levels escalate, more H_2O molecules are loosely adsorbed in a disordered manner with the adsorbed oxygen. The increasing amount of disordered adsorbed oxygen induces the formation of a high electrostatic field between the adsorbed layers, subsequently leading to the dissociation of H_2O molecules into H_3O^+ and OH^- ions by the following equation (eq 10):

$$H_2O \rightarrow H_3O^+ + OH^- \tag{10}$$

This dissociation process significantly enhances the proton conduction within the sensing layer. The abundance of water molecules in the sensing layer provides the proton with the freedom to hop within the water molecules, resulting in a reduction in sensor resistance. In the cross-sensitivity analysis, surface-adsorbed water molecules tend to solvate NH $_3$ gas into NH $^{4+}$ ions and actively react with adsorbed O $_2$ $^-$, further decreasing sensor resistance and increasing sensor response under highly humid conditions.

Therefore, the growth of edge-exposed ReS₂ nanosheets on the highly conductive and large surface area of Ti₃C₂T_x sheets provides numerous active sites for gas molecules and facilitates easy charge carrier transportation during the sensing process, thereby improving the gas sensing characteristics. Additionally, ReS₂ helps in preventing the oxidation degradation of the $Ti_3C_2T_r$ surface area and electrical properties. The presence of negative charge on the ReS2/Ti3C2Tx heterostructure due to the oxide and hydroxide terminal groups can further enhance the interaction with NH3 through the hydrogen bonding and electron donation mechanism, making this material more sensitive to NH₃. As a result, the synergistic effect of both ReS₂ and Ti₃C₂T_x leads to the synthesis of a stable ReS₂/Ti₃C₂T_x heterostructure, promoting more interaction between the sensing layer and target gas with faster gas adsorption/ desorption processes.

CONCLUSIONS

The present work demonstrates the remarkable sensing capabilities of a ReS₂/Ti₃C₂T_x heterostructure-based sensor for the detection of NH₃ in natural environmental conditions. The structural and morphological analysis of the heterostructure, fabricated through a one-pot hydrothermal method of ReS₂ on templating Ti₃C₂T_x sheets, revealed a uniform distribution of curvy and vertically oriented ReS2 nanosheets on the surface of Ti₃C₂T_x sheets, resulting in an increased specific surface area. The large surface area of $Ti_3C_2T_x$ along with the distorted 1T structure of ReS₂ exhibits an increased number of edge sites suitable for gas adsorption. This synergistic effect has led into a 1.3 times improvement in sensing response compared to pristine ReS₂ on exposure to 10 ppm of NH₃ at 15% RH and RT. Furthermore, the ReS₂/ Ti₃C₂T_x heterostructure showed excellent repeatability, longterm stability, and superior sensitivity (7.8-12.4%) toward NH₃ within the range of 15-85% RH. These findings collectively suggest that the ReS₂/Ti₃C₂T_x heterostructure

could be used as a promising sensing material for enhanced NH_3 detection in natural environmental conditions, contributing to the advancements in environmental monitoring and safety measures.

ASSOCIATED CONTENT

Supporting Information

The Supporting Information is available free of charge at https://pubs.acs.org/doi/10.1021/acssensors.4c01216.

Room-temperature MXene (${\rm Ti_3C_2T_x}$)-based sensor and its sensing performance toward ammonia (NH₃); image of the fabricated gas sensor; diffraction patterns of MXene and RM30; FESEM micrographs of the studied materials; EDX and elemental mappings; XPS; Raman spectroscopy supplemental data; BET supplemental data; I-V curves; resistance—time transient curves; selectivity data (PDF)

AUTHOR INFORMATION

Corresponding Author

Cheng-Yu Lai — Department of Mechanical and Materials Engineering, Florida International University, Miami, Florida 33174, United States; Department of Chemistry and Biochemistry, Florida International University, Miami, Florida 33199, United States; ⊙ orcid.org/0000-0002-8931-5601; Email: clai@fiu.edu

Authors

- Sahil Gasso Department of Mechanical and Materials Engineering, Florida International University, Miami, Florida 33174, United States
- Jake Carrier Department of Chemistry and Biochemistry, Florida International University, Miami, Florida 33199, United States
- Daniela Radu Department of Mechanical and Materials Engineering, Florida International University, Miami, Florida 33174, United States; orcid.org/0000-0001-6833-5825

Complete contact information is available at: https://pubs.acs.org/10.1021/acssensors.4c01216

Notes

The authors declare no competing financial interest.

ACKNOWLEDGMENTS

This work was supported in part by the National Science Foundation Award #DMR-2122078 and Department of Defense Awards #W911NF2210186, W911NF2320229, and W911NF2310152. The authors thank Prof. Titel Jurca at the University of Central Florida for his help with XPS data collection and Linisha Biswal at Florida International University for Raman data collection.

REFERENCES

- (1) Tang, N.; Zhou, C.; Xu, L.; Jiang, Y.; Qu, H.; Duan, X. A Fully Integrated Wireless Flexible Ammonia Sensor Fabricated by Soft Nano-Lithography. ACS Sensors 2019, 4 (3), 726–32.
- (2) Pattanarat, K.; Petchsang, N.; Osotchan, T.; Tang, I. M.; Kim, Y.-H.; Jaisutti, R. High Conductivity and Durability Textile Gas Sensor-Based Polyaniline-Decorated-Poly(3,4-ethylenedioxythiophene)/Poly(4-styrenesulfonate) for Ammonia Detection. ACS Applied Polymer Materials 2022, 4 (12), 9006–14.

- (3) Giddey, S.; Badwal, S. P. S.; Kulkarni, A. Review of electrochemical ammonia production technologies and materials. *Int. J. Hydrogen Energy* **2013**, *38* (34), 14576–94.
- (4) Saini, R.; Devi, P., 13 Nanosensors for detecting nutrient losses from soil (as gaseous ammonia and nitrous oxide, and/or soil leachates as nitrate and phosphate), In: Denizli, A.; Nguyen, T. A.; Rajendran, S.; Yasin, G.; Nadda, A. K. (Eds.), Nanosensors for Smart Agriculture; Elsevier 2022; pp 303–327.
- (5) Arkoti, N. K.; Pal, K. Selective Detection of NH $_3$ Gas by Ti $_3$ C $_2$ T $_x$ Sensors with the PVDF-ZIF-67 Overlayer at Room Temperature. ACS Sensors **2024**, *9*, 1465.
- (6) Kaur, R.; Gasso, S.; Saini, R. MXene-based highly sensitive and selective NH₃ sensor. *Journal of Physics: Conference Series* **2023**, 2518 (1), No. 012015.
- (7) Mani, G. K.; Rayappan, J. B. B. A highly selective and wide range ammonia sensor—Nanostructured ZnO:Co thin film. *Materials Science and Engineering: B* **2015**, *191*, 41–50.
- (8) Joshi, N.; Hayasaka, T.; Liu, Y.; Liu, H.; Oliveira, O. N.; Lin, L. A review on chemiresistive room temperature gas sensors based on metal oxide nanostructures, graphene and 2D transition metal dichalcogenides. *Microchimica Acta* **2018**, *185* (4), 213.
- (9) Joshi, N.; Braunger, M. L.; Shimizu, F. M.; Riul, A., Jr; Oliveira, O. N. Insights into nano-heterostructured materials for gas sensing: a review. *Multifunctional Materials* **2021**, *4* (3), No. 032002.
- (10) Preethichandra, D. M. G.; Gholami, M. D.; Izake, E. L.; O'Mullane, A. P.; Sonar, P. Conducting Polymer Based Ammonia and Hydrogen Sulfide Chemical Sensors and Their Suitability for Detecting Food Spoilage. *Advanced Materials Technologies* **2023**, 8 (4), 2200841.
- (11) Chen, X.; Yu, Y.; Yang, C.; Yin, J.; Song, X.; Li, J.; Fei, H. Fabrication of robust and porous Lead chloride-based metal—organic frameworks toward a selective and sensitive smart NH₃ sensor. *ACS Appl. Mater. Interfaces* **2021**, 13 (44), 52765–74.
- (12) Sohal, M. K.; Mahajan, A.; Gasso, S.; Nahirniak, S. V.; Dontsova, T. A.; Singh, R. C. Modification of SnO₂ surface oxygen vacancies through Er doping for ultralow NO₂ detection. *Mater. Res. Bull.* **2021**, *133*, No. 111051.
- (13) Dogra, N.; Kushvaha, S. S.; Sharma, S. Phase-Dependent Dual Discrimination of MoSe₂/MoO₃ Composites Toward N,N-Dimethylformamide and Triethylamine at Room Temperature. *ACS Sensors* **2023**, *8* (8), 3146–57.
- (14) Zappa, D.; Galstyan, V.; Kaur, N.; Munasinghe Arachchige, H. M. M.; Sisman, O.; Comini, E. Metal oxide -based heterostructures for gas sensors"- A review. *Anal. Chim. Acta* **2018**, *1039*, 1–23.
- (15) Liu, X.; Cheng, S.; Liu, H.; Hu, S.; Zhang, D.; Ning, H. A survey on gas sensing technology. *Sensors* **2012**, *12* (7), 9635–65.
- (16) Peng, X.; Wu, X.; Yang, F.; Tian, Y.; Zhang, M.; Yuan, H. Gas sensors based on metal-organic frameworks: Challenges and opportunities. *Chinese Journal of Structural Chemistry* **2024**, 43, No. 100251.
- (17) Gasso, S.; Sohal, M. K.; Mahajan, A. MXene modulated SnO_2 gas sensor for ultra-responsive room-temperature detection of NO_2 . Sens. Actuators, B **2022**, 357, No. 131427.
- (18) Joseph, S.; Mohan, J.; Lakshmy, S.; Thomas, S.; Chakraborty, B.; Thomas, S.; Kalarikkal, N. A review of the synthesis, properties, and applications of 2D transition metal dichalcogenides and their heterostructures. *Mater. Chem. Phys.* **2023**, 297, No. 127332.
- (19) Venkatesan, A.; Ryu, H.; Devnath, A.; Yoo, H.; Lee, S. Airstable, all-dry transferred ReS₂/GaSe heterostructure-based NO₂ gas sensor. *Journal of Materials Science & Technology* **2024**, *168*, 79–87.
- (20) Tabata, H.; Matsuyama, H.; Goto, T.; Kubo, O.; Katayama, M. Visible-Light-Activated Response Originating from Carrier-Mobility Modulation of NO₂ Gas Sensors Based on MoS₂ Monolayers. ACS Nano 2021, 15 (2), 2542–53.
- (21) Park, J.; Rautela, R.; Alzate-Carvajal, N.; Scarfe, S.; Scarfe, L.; Alarie, L.; Luican-Mayer, A.; Ménard, J.-M. UV Illumination as a Method to Improve the Performance of Gas Sensors Based on Graphene Field-Effect Transistors. ACS Sensors 2021, 6 (12), 4417—24.

- (22) Rahman, M.; Davey, K.; Qiao, S. Z. Advent of 2D rhenium disulfide (ReS₂): fundamentals to applications. *Adv. Funct. Mater.* **2017**, 27 (10), No. 1606129.
- (23) He, Q.; Zhou, J.; Tang, W.; Hao, Y.; Sun, L.; Zhu, C.; Xu, F.; Chen, J.; Wu, Y.; Wu, Z.; Xu, B.; Liu, G.; Li, X.; Zhang, C.; Kang, J. Deeply exploring anisotropic evolution toward large-scale growth of monolayer ReS₂. ACS Appl. Mater. Interfaces **2019**, 12 (2), 2862–2870.
- (24) Chenet, D. A.; Aslan, B.; Huang, P. Y.; Fan, C.; van der Zande, A. M.; Heinz, T. F.; Hone, J. C. In-Plane Anisotropy in Mono- and Few-Layer ReS₂ Probed by Raman Spectroscopy and Scanning Transmission Electron Microscopy. *Nano Lett.* **2015**, *15* (9), 5667–72.
- (25) Zhao, Y.; Li, J.; Huang, J.; Feng, L.; Cao, L.; Feng, Y.; Zhang, Z.; Xie, Y.; Wang, H. Controlled Growth of Edge-Enriched ReS₂ Nanoflowers on Carbon Cloth Using Chemical Vapor Deposition for Hydrogen Evolution. *Adv. Mater. Interfaces* **2020**, 7 (22), No. 2001196.
- (26) Yang, A.; Gao, J.; Li, B.; Tan, J.; Xiang, Y.; Gupta, T.; Li, L.; Suresh, S.; Idrobo, J. C.; Lu, T.-M.; et al. Humidity sensing using vertically oriented arrays of ReS₂ nanosheets deposited on an interdigitated gold electrode. 2D Materials 2016, 3 (4), No. 045012.
- (27) Goel, N.; Utkarsha; Kushwaha, A.; Kwoka, M.; Kumar, R.; Kumar, M. Mixed-dimensional van der Waals heterostructures enabled gas sensors: Fundamentals and Applications. *J. Mater. Chem. A* **2024**, *12*, 5642.
- (28) Wu, R.; Yan, K.; Zhao, J.; Cai, Z.; Jian, S.; Qiu, L. 2D/2D SnS₂/SnSe₂ van der Waals heterostructure for highly sensitive room-temperature NO₂ sensor: Key role of interface contact. *Chemical Engineering Journal* **2023**, 466, No. 143369.
- (29) Liu, X.; Wang, M.; Qin, B.; Zhang, Y.; Liu, Z.; Fan, H. 2D-2D MXene/ReS₂ hybrid from Ti₃C₂T_x MXene conductive layers supporting ultrathin ReS₂ nanosheets for superior sodium storage. *Chemical Engineering Journal* **2022**, 431, No. 133796.
- (30) Dogra, N.; Gasso, S.; Sharma, A.; Sharma, K. K.; Sharma, S. TiO₂ decorated MXene nanosheets for high-performance ammonia gas sensing at room-temperature. *Surfaces and Interfaces* **2024**, 48, No. 104290.
- (31) Yu, H.; Dai, L.; Liu, Y.; Zhou, Y.; Fan, P.; Luo, J.; Zhong, A. Ti₃C₂Tx MXene-SnO₂ nanocomposite for superior room temperature ammonia gas sensor. *J. Alloys Compd.* **2023**, *962*, No. 171170.
- (32) Gasso, S.; Mahajan, A. MXene based 2D-2D heterostructures for Counter Electrode in third generation Dye Sensitized Solar Cells. *Chem. Phys. Lett.* **2022**, 808, No. 140144.
- (33) Iqbal, A.; Hong, J.; Ko, T. Y.; Koo, C. M. Improving oxidation stability of 2D MXenes: synthesis, storage media, and conditions. *Nano Convergence* **2021**, *8* (1), 9.
- (34) Zhao, X.; Vashisth, A.; Prehn, E.; Sun, W.; Shah, S. A.; Habib, T.; Chen, Y.; Tan, Z.; Lutkenhaus, J. L.; Radovic, M.; Green, M. J. Antioxidants unlock shelf-stable Ti₃C₂Tx (MXene) nanosheet dispersions. *Matter* **2019**, *1* (2), 513–526.
- (35) Zhou, Q.; Luo, S.; Xue, W.; Liao, N. Highly selective nitrogen dioxide gas sensing of ReS₂ nanosheets: A first-principles study. *Appl. Surf. Sci.* **2023**, *609*, No. 155388.
- (36) Khakbaz, P.; Moshayedi, M.; Hajian, S.; Soleimani, M.; Narakathu, B. B.; Bazuin, B. J.; Pourfath, M.; Atashbar, M. Z. Titanium carbide MXene as NH₃ sensor: realistic first-principles study. *J. Phys. Chem. C* **2019**, 123 (49), 29794–803.
- (37) Tian, X.; Yao, L.; Cui, X.; Zhao, R.; Chen, T.; Xiao, X.; Wang, Y. A two-dimensional Ti₃C₂T_XMXene@TiO₂/MoS₂ heterostructure with excellent selectivity for the room temperature detection of ammonia. *Journal of Materials Chemistry A* **2022**, *10* (10), 5505–19.
- (38) Liu, S.; Wang, M.; Liu, G.; Wan, N.; Ge, C.; Hussain, S.; Meng, H.; Wang, M.; Qiao, G. Enhanced NO₂ gas-sensing performance of 2D Ti₃C₂/TiO₂ nanocomposites by in-situ formation of Schottky barrier. *Appl. Surf. Sci.* **2021**, *567*, No. 150747.
- (39) Lukatskaya, M. R.; Kota, S.; Lin, Z.; Zhao, M.-Q.; Shpigel, N.; Levi, M. D.; Halim, J.; Taberna, P.-L.; Barsoum, M. W.; Simon, P.; et al. Ultra-high-rate pseudocapacitive energy storage in two-

- dimensional transition metal carbides. Nature Energy 2017, 2 (8), 17105.
- (40) Na, H.; Venedicto, M.; Chang, C.-Y.; Carrier, J.; Lai, C.-Y. Infrared-Activated Bactericide: Rhenium Disulfide (ReS₂)-Functionalized Mesoporous Silica Nanoparticles. *ACS Applied Bio Materials* **2023**, *6* (4), 1577–85.
- (41) Qi, F.; He, J.; Chen, Y.; Zheng, B.; Li, Q.; Wang, X.; Yu, B.; Lin, J.; Zhou, J.; Li, P.; et al. Few-layered ReS₂ nanosheets grown on carbon nanotubes: A highly efficient anode for high-performance lithium-ion batteries. *Chemical Engineering Journal* **2017**, 315, 10–7.
- (42) Zhang, K.; Di, M.; Fu, L.; Deng, Y.; Du, Y.; Tang, N. Enhancing the magnetism of 2D carbide MXene $Ti_3C_2T_x$ by H_2 annealing. *Carbon* **2020**, 157, 90–6.
- (43) Gasso, S.; Kaur Sohal, M.; Chand Singh, R.; Mahajan, A. NOx sensor based on semiconductor metal oxide and MXene nanostructures. *Materials Today: Proceedings* **2023**, *92*, 632–5.
- (44) Chen, L.; Cao, Y.; Zhang, X.; Guo, X.; Song, P.; Chen, K.; Lin, J. Anisotropic and high thermal conductivity of epoxy composites containing multilayer ${\rm Ti}_3{\rm C}_2{\rm T}_{\rm x}$ MXene nanoflakes. *J. Mater. Sci.* **2020**, *55*, 16533–43.
- (45) Gasso, S.; Mahajan, A. MXene decorated tungsten trioxide nanocomposite-based sensor capable of detecting NO₂ gas down to ppb-level at room temperature. *Materials Science in Semiconductor Processing* **2022**, *152*, No. 107048.
- (46) Zhou, X.; Li, Y.; Huang, Q. Preparation of $Ti_3C_2T_x/NiZn$ ferrite hybrids with improved electromagnetic properties. *Materials* **2020**, *13* (4), 820.
- (47) Gasso, S.; Mahajan, A. Self-Powered Wearable Gas Sensors Based on l-Ascorbate-Treated MXene Nanosheets and SnO₂ Nanofibers. ACS Applied Nano Materials **2023**, 6 (8), 6678–92.
- (48) Wang, X.; Chen, B.; Yan, D.; Zhao, X.; Wang, C.; Liu, E.; Zhao, N.; He, F. Distorted 1T-ReS₂ Nanosheets Anchored on Porous TiO₂ Nanofibers for Highly Enhanced Photocatalytic Hydrogen Production. *ACS Appl. Mater. Interfaces* **2019**, *11* (26), 23144–51.
- (49) Zhan, X.; Ou, D.; Zheng, Y.; Li, B.; Xu, L.; Yang, H.; Yang, W.; Zhang, H.; Hou, H.; Yang, W. Boosted photocatalytic hydrogen production over two-dimensional/two-dimensional Ta₃N₅/ReS₂ van der Waals heterojunctions. *J. Colloid Interface Sci.* **2023**, *629*, 455–66.
- (50) Ahmed, B.; Anjum, D. H.; Hedhili, M. N.; Gogotsi, Y.; Alshareef, H. N. H₂O₂ assisted room temperature oxidation of Ti₂C MXene for Li-ion battery anodes. *Nanoscale* **2016**, *8* (14), 7580–7.
- (51) Liu, S.; Liu, Y.; Lei, W.; Zhou, X.; Xu, K.; Qiao, Q.; Zhang, W.-H. Few-layered ReS₂ nanosheets vertically aligned on reduced graphene oxide for superior lithium and sodium storage. *Journal of Materials Chemistry A* **2018**, 6 (41), 20267–76.
- (52) Mao, M.; Cui, C.; Wu, M.; Zhang, M.; Gao, T.; Fan, X.; Chen, J.; Wang, T.; Ma, J.; Wang, C. Flexible ReS₂ nanosheets/N-doped carbon nanofibers-based paper as a universal anode for alkali (Li, Na, K) ion battery. *Nano Energy* **2018**, *45*, 346–52.
- (53) Zhuo, Z.; Zhu, J.; Wei, A.; Liu, J.; Luo, N.; Zhao, Y.; Liu, Z. Electrocatalytic performance of ReS₂ nanosheets in hydrogen evolution reaction. *Int. J. Hydrogen Energy* **2022**, 47 (4), 2293–303.
- (54) Kalambate, P. K.; Dhanjai; Sinha, A.; Li, Y.; Shen, Y.; Huang, Y. An electrochemical sensor for ifosfamide, acetaminophen, domperidone, and Sumatriptan based on self-assembled MXene/MWCNT/chitosan nanocomposite thin film. *Microchim. Acta* **2020**, *187*, 1–12.
- (55) Halim, J.; Cook, K. M.; Naguib, M.; Eklund, P.; Gogotsi, Y.; Rosen, J.; Barsoum, M. W. X-ray photoelectron spectroscopy of select multi-layered transition metal carbides (MXenes). *Appl. Surf. Sci.* **2016**, *362*, 406–17.
- (56) Zhu, H.; Xue, Q.; Zhu, G.; Liu, Y.; Dou, X.; Yuan, X. Decorating Pt@ cyclodextrin nanoclusters on $C_3N_4/MXene$ for boosting the photocatalytic H_2O_2 production. *Journal of Materials Chemistry A* **2021**, 9 (11), 6872–80.
- (57) Liu, S.; Lei, W.; Liu, Y.; Zhang, W.-H. Uniform ReS₂ porous nanospheres assembled from curly ReS₂ few-layers with an expanded interlayer spacing for high-performance lithium-ion batteries. *Chemical Engineering Journal* **2019**, 357, 112–9.

- (58) Wang, L.; Zhang, H.; Wang, B.; Shen, C.; Zhang, C.; Hu, Q.; Zhou, A.; Liu, B. Synthesis and electrochemical performance of $Ti_3C_2T_x$ with hydrothermal process. *Electronic Materials Letters* **2016**, 12, 702–10.
- (59) Ranjbar, F.; Hajati, S.; Ghaedi, M.; Dashtian, K.; Naderi, H.; Toth, J. Highly selective $MXene/V_2O_5/CuWO_4$ -based ultra-sensitive room temperature ammonia sensor. *Journal of Hazardous Materials* **2021**, *416*, No. 126196.
- (60) Lee, E.; VahidMohammadi, A.; Prorok, B. C.; Yoon, Y. S.; Beidaghi, M.; Kim, D.-J. Room temperature gas sensing of two-dimensional titanium carbide (MXene). *ACS Appl. Mater. Interfaces* **2017**, *9* (42), 37184–90.
- (61) Mustakeem, M.; El-Demellawi, J. K.; Obaid, M.; Ming, F.; Alshareef, H. N.; Ghaffour, N. MXene-Coated Membranes for Autonomous Solar-Driven Desalination. ACS Appl. Mater. Interfaces 2022, 14 (4), 5265–74.
- (62) Spanier, J. E.; Gupta, S.; Amer, M.; Barsoum, M. W. Vibrational behavior of the $M_{\rm n+1}AX_{\rm n}$ phases from first-order Raman scattering (*M*=Ti, V, Cr, $A={\rm Si},~X={\rm C},~{\rm N}$). *Phys. Rev. B* **2005**, 71 (1), No. 012103.
- (63) Hu, T.; Wang, J.; Zhang, H.; Li, Z.; Hu, M.; Wang, X. Vibrational properties of Ti_3C_2 and $Ti_3C_2T_2$ (T=O,F,OH) monosheets by first-principles calculations: a comparative study. *Phys. Chem. Chem. Phys.* **2015**, *17* (15), 9997–10003.
- (64) Sarycheva, A.; Makaryan, T.; Maleski, K.; Satheeshkumar, E.; Melikyan, A.; Minassian, H.; Yoshimura, M.; Gogotsi, Y. Two-Dimensional Titanium Carbide (MXene) as Surface-Enhanced Raman Scattering Substrate. *J. Phys. Chem. C* **2017**, *121* (36), 19983–8.
- (65) Sengupta, A.; Rao, B. V. B.; Sharma, N.; Parmar, S.; Chavan, V.; Singh, S. K.; Kale, S.; Ogale, S. Comparative evaluation of MAX, MXene, NanoMAX, and NanoMAX-derived-MXene for microwave absorption and Li ion battery anode applications. *Nanoscale* **2020**, *12* (15), 8466–76.
- (66) Gasso, S.; Mahajan, A. Development of Highly Sensitive and Humidity Independent Room Temperature NO₂ Gas Sensor Using Two Dimensional Ti₃C₂Tx Nanosheets and One Dimensional WO₃ Nanorods Nanocomposite. ACS sensors 2022, 7 (8), 2454–64.
- (67) Li, X.; Yin, X.; Han, M.; Song, C.; Xu, H.; Hou, Z.; Zhang, L.; Cheng, L. Ti₃C₂ MXenes modified with in situ grown carbon nanotubes for enhanced electromagnetic wave absorption properties. *Journal of Materials Chemistry C* **2017**, 5 (16), 4068–74.
- (68) Zhang, Q.; Tan, S.; Mendes, R. G.; Sun, Z.; Chen, Y.; Kong, X.; Xue, Y.; Rümmeli, M. H.; Wu, X.; Chen, S.; et al. Extremely Weak van der Waals Coupling in Vertical ReS₂ Nanowalls for High-Current-Density Lithium-Ion Batteries. *Adv. Mater.* **2016**, 28 (13), 2616–23.
- (69) Gao, H.; Yue, H.-H.; Qi, F.; Yu, B.; Zhang, W.-L.; Chen, Y.-F. Few-layered ReS₂ nanosheets grown on graphene as electrocatalyst for hydrogen evolution reaction. *Rare Metals* **2018**, *37* (12), 1014–20.
- (70) Qi, F.; Chen, Y.; Zheng, B.; Zhou, J.; Wang, X.; Li, P.; Zhang, W. Facile growth of large-area and high-quality few-layer ReS₂ by physical vapour deposition. *Mater. Lett.* **2016**, *184*, 324–7.
- (71) Dhenadhayalan, N.; Lin, T.-W.; Veerakumar, P.; Lin, K.-C. Metal Nanoparticles Anchored on Rhenium Disulfide Nanosheets as Catalysts for the Reduction of Aromatic Nitro Compounds. *ChemNanoMat* **2018**, *4* (12), 1262–9.
- (72) Shi, C.; Liu, Z.; Tian, Z.; Li, D.; Chen, Y.; Guo, L.; Wang, Y. Regulated layer spacing and functional surface group of MXene film by hexamethylenetetramine for high-performance supercapacitors. *Appl. Surf. Sci.* **2022**, *596*, No. 153632.
- (73) Hermawan, A.; Zhang, B.; Taufik, A.; Asakura, Y.; Hasegawa, T.; Zhu, J.; Shi, P.; Yin, S. CuO Nanoparticles/Ti₃C₂T_x MXene Hybrid Nanocomposites for Detection of Toluene Gas. *ACS Applied Nano Materials* **2020**, *3* (5), 4755–66.
- (74) Sadhanala, H. K.; Nandan, R.; Nanda, K. K. Understanding the ammonia sensing behavior of filter coffee powder derived N-doped carbon nanoparticles using the Freundlich-like isotherm. *Journal of Materials Chemistry A* **2016**, 4 (22), 8860–5.

- (75) Nam, M. S.; Kim, J.-Y.; Mirzaei, A.; Lee, M. H.; Kim, H. W.; Kim, S. S. Au- and Pt-decorated Ti₃C₂T_x MXenes for preparing self-heated and flexible NH₃ gas sensors. *Sens. Actuators, B* **2024**, 403, No. 135112.
- (76) Adepu, V.; Bokka, N.; Mattela, V.; Sahatiya, P. A highly electropositive ReS₂ based ultra-sensitive flexible humidity sensor for multifunctional applications. *New J. Chem.* **2021**, *45* (13), 5855–62.
- (77) Park, J. Y.; Joe, H.-E.; Yoon, H. S.; Yoo, S.; Kim, T.; Kang, K.; Min, B.-K.; Jun, S. C. Contact Effect of ReS₂/Metal Interface. ACS Appl. Mater. Interfaces **2017**, 9 (31), 26325–32.
- (78) Kale, S.; Parmar, S.; Datar, S.; Kale, S. Tuneable work function of titanium carbide $(Ti_3C_2T_x)$ by modification in surface termination groups. *Mater. Chem. Phys.* **2023**, *306*, No. 128052.
- (79) He, T.; Liu, W.; Lv, T.; Ma, M.; Liu, Z.; Vasiliev, A.; Li, X. MXene/SnO₂ heterojunction based chemical gas sensors. *Sens. Actuators, B* **2021**, 329, No. 129275.
- (80) Liu, Z.; He, T.; Sun, H.; Huang, B.; Li, X. Layered MXene heterostructured with In_2O_3 nanoparticles for ammonia sensors at room temperature. *Sens. Actuators, B* **2022**, *365*, No. 131918.
- (81) Gupta, A.; Sakhuja, N.; Jha, R. K.; Bhat, N. Ultrasensitive chemiresistive humidity sensor based on gold functionalized WS₂ nanosheets. *Sensors and Actuators A: Physical* **2021**, 331, No. 113008.